

Accurate estimates of land surface energy fluxes and irrigation requirements from UAV-based thermal and multispectral sensors

Junxiang Peng^{a,b,e,*}, Hector Nieto^{c,d}, Mathias Neumann Andersen^a, Kirsten Kørup^a,
Rene Larsen^a, Julien Morel^e, David Parsons^e, Zhenjiang Zhou^{b,f,*}, Kiril Manevski^{a,*}

^a Department of Agroecology, Aarhus University, Blichers Allé 50, 8830 Tjele, Denmark

^b College of Biosystems Engineering and Food Science, Zhejiang University, Hangzhou 310058, China

^c Institute of Agricultural Sciences - ICA-CSIC. Tec4AGRO Group. Serrano 115b, Madrid 28006, Spain

^d Efficient Use of Water in Agriculture Program, Institute of AgriFood, Research and Technology (IRTA), Parc Científic i Tecnològic Agroalimentari de Gardeny, Fruitcentre, 25003 Lleida, Spain

^e Department of Crop Production Ecology, Swedish University of Agricultural Sciences, 90183 Umeå, Sweden

^f Huanan Industrial Technology Research Institute of Zhejiang University, Guangzhou 510700, China

ARTICLE INFO

Keywords:

Drought stress
Evapotranspiration
Potato
Sap flow
Two system energy balance
Unmanned aerial vehicle

ABSTRACT

The two-source energy balance model estimates canopy transpiration (T_r) and soil evaporation (E) traditionally from satellite partitions of remotely sensed land surface temperature (LST) and the Priestley-Taylor equation (TSEB-PT) at seasonal time with limited accuracy. The high spatial-temporal resolution spectral data collected by unmanned aerial vehicles (UAVs) provide valuable opportunity to estimate T_r and E precisely, improve the understanding of the seasonal and the diurnal cycle of evapotranspiration (ET), and timely detect agricultural drought. The UAV data vary in spatial resolution and the uncertainty imposed on the TSEB-PT outcome has thus far not been considered. To address these challenges and prospects, a new energy flux modelling framework based on TSEB-PT for high spatial resolution thermal and multispectral UAV data is proposed in this paper. Diurnal variations of LST in agricultural fields were recorded with a thermal infrared camera installed on an UAV during drought in 2018 and 2019. Observing potato as a test crop, LST , plant biophysical parameters derived from corresponding UAV multispectral data, and meteorological forcing variables were employed as input variables to TSEB-PT. All analyses were conducted at different pixelation of the UAV data to quantify the effect of spatial resolution on the performance. The 1 m spatial resolution produced the highest correlation between T_r modelled by TSEB-PT and measured by sap flow sensors ($R^2 = 0.80$), which was comparable to the 0.06, 0.1, 0.5 and 2 m pixel sizes ($R^2 = 0.76$ – 0.78) and markedly higher than the lower resolutions of 2 to 24 m ($R^2 = 0.30$ – 0.72). Modelled T_r was highly and significantly correlated with measured leaf water potential ($R^2 = 0.81$) and stomatal conductance ($R^2 = 0.74$). The computed irrigation requirements (IR s) reflected the field irrigation treatments, ET and conventional irrigation practices in the area with high accuracy. It was also found that using a net primary production model with explicit representation of temperature influences made it possible to distinguish effects of drought *vis-a-vis* heat stress on crop productivity and water use efficiency. The results showed excellent model performance for retrieving T_r and ET dynamics under drought stress and proved that the proposed remote sensing based TSEB-PT framework at UAV scale is a promising tool for the investigation of plant drought stress and water demand; this is particularly relevant for local and regional irrigations scheduling.

1. Introduction

Amid the global climate crisis due to greenhouse gas emissions, changing patterns in temperature and precipitation, and irrigation water overuse (Wada et al., 2010), accurate estimations of surface energy

fluxes are critical for determining agronomic drought and crop water demand in precision agriculture (Kustas and Anderson, 2009). Latent heat flux (LE , $W m^{-2}$), i.e., dissipating heat from the surface to the atmosphere by water evaporation, is the key process determining the water balance and the biogeochemical function of ecosystems (Mallick

* Corresponding authors.

E-mail addresses: junxiang.peng@slu.se, pengjunxiang21@163.com (J. Peng), zhenjiangz@zju.edu.cn (Z. Zhou), kiril.manevski@agro.au.dk (K. Manevski).

<https://doi.org/10.1016/j.isprsjprs.2023.03.009>

Received 24 July 2022; Received in revised form 6 March 2023; Accepted 10 March 2023

Available online 28 March 2023

0924-2716/© 2023 The Author(s). Published by Elsevier B.V. on behalf of International Society for Photogrammetry and Remote Sensing, Inc. (ISPRS). This is an open access article under the CC BY license (<http://creativecommons.org/licenses/by/4.0/>).

et al., 2009). Evapotranspiration (ET ; mm), the equivalent to LE in terms of rate of water use, transfers water from soil (evaporation, E) and plant (transpiration, Tr) as vapor to the atmosphere with a concurrent removal of energy from the land surface (Maes and Steppe, 2012). It can be calculated by dividing LE with the latent heat of vaporization and density of water. From an agro-environmental perspective, ET can be used for scheduling irrigation and managing water use. The spatio-temporal distribution of the surface energy balance, and hence of ET , remain challenging to estimate due to, among others, variability of soil water storage, root depth, plant water status and leaf conductance over time, all of which affect ET . Methods are therefore needed to improve the estimation of ET and take its subtle spatial variability into account.

Eddy covariance flux tower is a reliable micro-meteorological tool to measure LE (Fisher et al., 2009; Twine et al., 2000), but with obvious shortcomings when retrieving spatial heat flux distribution over heterogeneous fields (Yao et al., 2015), in addition to being instrumentally expensive and computationally complex. Alternatively, LE can be estimated by remote sensing, as the residual of the surface energy balance involving net radiation (R_n), sensible heat flux (H) and soil heat flux (G) assuming no other energy terms or apparent heat advection (Hoffmann et al., 2016; Morillas et al., 2013); R_n , H and G are calculated from either ground or remote measurements alongside local meteorology (Gowda et al., 2008). The two-source energy balance (TSEB) model proposed by Norman et al. (1995) and further developed by Kustas and Norman (1999) separates the remotely sensed land surface temperature (LST) into canopy and soil temperatures and compared to a one-source surface heat flux (Verhoef et al., 1997), it estimates fluxes more robustly for heterogeneous fields under a wider range of environmental conditions (Kustas and Norman, 1999). The flux partitioning is based on an iterative process initiated by an estimate of a potential (maximal) Tr computed by the Priestley-Taylor approximation (Priestley and Taylor, 1972; hence, the abbreviation TSEB-PT). The exchange of heat between the two sources (soil and canopy) and the atmosphere is modulated by a series of “resistances” (an analogue to the resistances in electrical systems that describe how heat and water vapour exchange is enhanced/opposed through the air, due to turbulence and atmospheric stability), being dependent on aerodynamic and meteorological conditions (Guzinski and Nieto, 2019). Accurate estimation of the fraction of green (transpiring) canopy and leaf area index (LAI) is particularly important for TSEB-PT to initiate the first guess of potential Tr , therefore, R_n , H and G of plant and soil are estimated separately. The TSEB model has been applied on data from several common open-access satellites platforms providing thermal infrared imagery, such as the Moderate Resolution Imaging Spectroradiometer (MODIS), Landsat-8 and Sentinel-3 (Anderson et al., 2011; Anderson et al., 2004; Andreu et al., 2018; Guzinski and Nieto, 2019), which typically have relatively coarse spatial resolution for agro-environmental studies and hamper precise results at sub-field level. Unmanned aerial vehicles (UAVs), on the other hand, add value in this regard due to the finer spatial resolution of the data they provide and thus the possibility to more precisely delineate canopy and soil components, thereby reducing the uncertainty of separating signals from mixed pixels (Nieto et al., 2019; Wang et al., 2019; Hoffmann et al., 2016).

Detecting in-season plant water needs requires appropriate spatial, spectral and temporal resolution of the data. Diurnal covariation in R_n and G affects the surface energy balance. For instance an irrigation or rainfall event reduces LST while increasing E and Tr (Knipper et al., 2019). The extent to which irrigation affects the re-partitioning of the sensible and the latent heat fluxes during the day remains poorly understood and, to our knowledge, diurnal variation of ET for agricultural fields based on TSEB-PT and UAV data and potentials have not been described yet. Furthermore, there is a lack of knowledge on whether and to what extent UAV-based estimates of ET can be applied to define and operationalize irrigation requirements (IRs).

The main aim of this study was to design a plausible framework for quantifying plant and soil energy fluxes based on remotely sensed LST

and TSEB-PT. The study was conducted in Denmark during July in both 2018 (the European drought and heat wave, thus under ideal conditions for studying drought) and 2019, on experimental fields cultivated with potato (*Solanum tuberosum* var. Oleva). Modelling of ET with remote sensing over potato fields has not been performed before, as the plant is drought and heat sensitive, and thus is usually grown under temperate and non-drought stressed conditions (Hijmans, 2003; Zhou et al., 2017; Peng et al., 2021a). Therefore, potato may globally be less exposed, but more sensitive to these abiotic stresses compared to other crops, such as maize, rice or wheat. The objectives of the study were to: i) evaluate the estimated Tr against hourly sap flow measurements and quantify the effect of spatial resolution on the quality of the estimated fluxes, ii) estimate diurnal ET from UAV LST images based on TSEB-PT modelling with explicit spatio-temporal estimation of Tr and E , and evaluate the correlation between Tr and plant biophysical variables, and iii) determine water use efficiency (WUE) and IR and investigate their accuracy.

2. Materials and Methods

2.1. Study site, experimental design and field data collection

The detailed workflow of the framework for calculating the water fluxes and eventually IR consisted of a field experiment and a remote sensing campaign, as shown in Fig. 1. The field experiment was conducted in the summers of 2018 and 2019 in central Denmark (56°31'59.6"N, 9°24'39.4"E) on a coarse sandy soil. The climate is temperate and humid, with moderately warm summers, cool to cold winters and low seasonal temperature variation. The weather in 2018 was unusually warm and dry, with corresponding mean temperatures and precipitation at the experimental site from 1 June to 31 August of 18 °C and 154 mm, compared to the respective mean values for the past 15 years of 15 °C and 205 mm. The weather in 2019 was relatively normal, though wetter, with summer mean temperature and precipitation of 17 °C and 357 mm, respectively. Meteorological data (air temperature and pressure, wind speed, relative humidity, long- and shortwave irradiance) were collected from a nearby meteorological station 500 m away from the experimental site (56°31'51.75"N, 9°24'40.99"E). Apart from these meteorological parameters, dew point was calculated using the “humidity.to.dewpoint” function from the “weathermetrics” package (Anderson and Peng, 2012) in R (ver. 3.5.1; R Core Team, 2013). Potato was planted in early May in 2018 and 2019. The experiments were conducted with a complete randomized block design comprising two factors: irrigation at full, deficit and low rates, and nitrogen (N) fertilizer rates of either full or variable, with four replicates. Further details about the field setup are provided in Peng et al. (2021a, b). This study focused on two plots (30 × 30 m²) of full N fertilization, but contrasting irrigation, i.e., full and low (Fig. 2), for the period when daily maximum temperature exceeded 20 °C, which is above the 17.2 °C cardinal maximum temperature for optimal potato growth (Peng et al., 2021a). The study periods including the remote sensing campaign were from 2 to 24 July in 2018 and 10 to 26 July in 2019. The date interval was weekly to slightly flexible (+/- few days) depending on the weather forecast when the temperature was high, so there was possibility for drought.

Soil water content (SWC) was measured weekly by time domain reflectometry (TDR-100 box; Campbell Scientific, Logan, Utah, USA) connected to a handheld computer (Allegro, Juniper Systems, Inc. Logan, Utah, USA) for trace interpretation. The TDR probes were installed in the center of each plot vertically to 60 cm depth, midway between the top of the ridge and the bottom of the furrow, in order to measure root zone SWC (0–60 cm). Details of the probe design and TDR-trace interpretation software are given by Thomsen (1994), and soil moisture content calculations were made according to Shahnazari et al. (2007). The field capacity (FC) was determined as SWC before emergence of the potatoes, five days after the soil had been thoroughly wetted by rain and subsequently drained off (Hillel, 2003). The soil

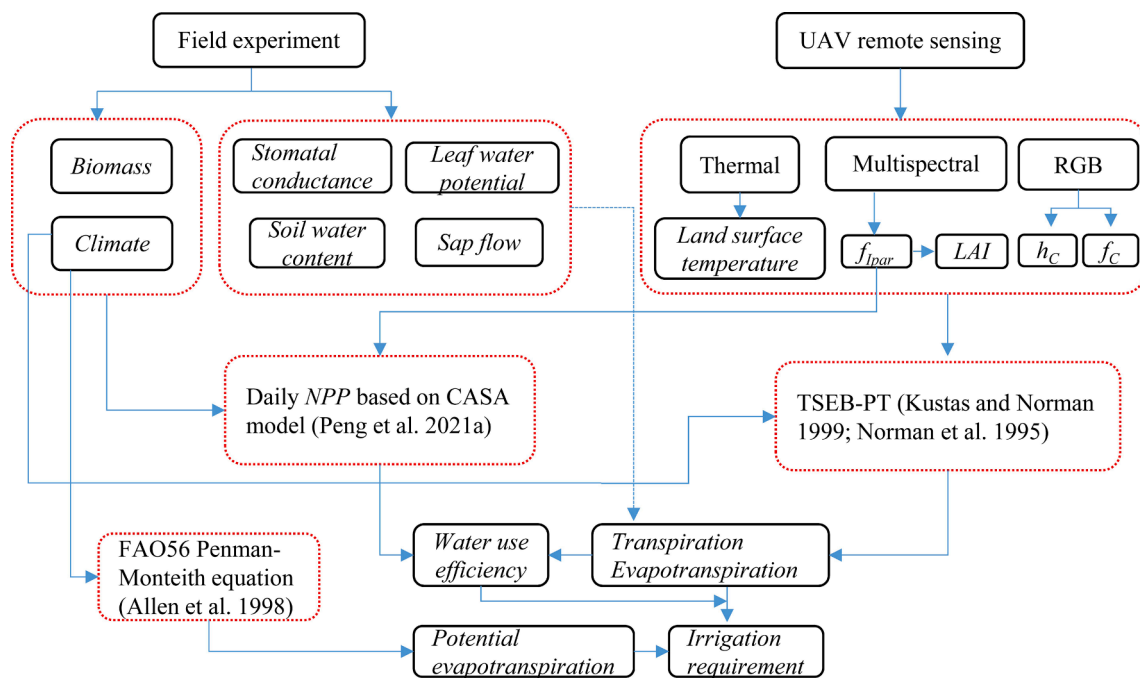


Fig. 1. Workflow in the framework for quantifying water fluxes in agroecosystem based on a two-source energy balance model with Priestley-Taylor approximation (TSEB-PT). The framework consists of a field campaign measuring climatic and plant variables for calculation of net primary productivity (NPP) with the light use efficiency (CASA) model, and a remote sensing campaign at unmanned aerial vehicle (UAV) scale. f_{lpar} , LAI, h_c , and f_c are fraction of intercepted photosynthetically active radiation, leaf area index, height of canopy, and fraction of cover, respectively.



Fig. 2. Location of the study site in Denmark (A) and layouts of the experimental plots in 2018 (B) and 2019 (C). Solid and dashed squares in the panels B and C indicate full and low irrigation treatments, respectively. Circles and triangles show, respectively, the positions of the time domain reflectometers (TDR; Campbell Scientific, Logan, Utah, USA) used for soil water content (SWC) measurements and sap flow sensors measuring plant transpiration. Backgrounds in B and C are RGB images recorded on 24 July 2018 and 26 July 2019. Legend and scale apply for panels B and C. (For interpretation of the references to colour in this figure legend, the reader is referred to the web version of this article.)

water deficit (SWD) was calculated as the difference between the weekly measured SWC and SWC at FC. The SWD was used to schedule irrigation in the fully irrigated treatment whenever 40–50 % of the available water capacity (i.e. 25–30 mm) was used.

Sap flow data were collected at 10-minute intervals by SGA13-WS Dynagage sensors (Dynamax, Houston, Tx, USA) installed on four shoots per plot from 6 July to 6 September in 2018 and from 24 July to 11 August in 2019. The sensors were installed 4 to 8 m from the plots border in order to ensure connectivity from multiple plots to a CR1000 data logger (Campbell Scientific, Logan, UT, USA) running the Dynamax Flow32A-1 K software. The variance of the plant transpiration measured by sap flow sensors was assumed to represent the variance of the plot

since the management actions (sowing, fertilization, irrigation, pests and diseases control) in each treatment plot were applied evenly by machinery. In 2018, four additional sensors were installed in the full irrigation plot on 19 July and another four sensors were installed on 16 July in another low irrigation treatment plot (Fig. 2). Other measurements included leaf stomatal conductance (g_s , mol m⁻² s⁻¹) and leaf water potential (LWP, MPa) recorded diurnally. Leaf stomatal conductance was measured on both the abaxial and the adaxial surface of a fully developed leaf (4th, 5th and 6th leaf counting upwards) on three plants per plot using a calibrated leaf porometer (SC-1, Decagon, Pullman, WA, USA). LWP was measured on the same leaflet immediately after the g_s measurement by enclosing it in a plastic bag before cutting the petiole

with a razor blade. The leaflet inside the plastic bag was quickly enclosed in a pressure chamber (Soil Moisture Equipment, Santa Barbara, CA, USA) and slowly pressurized. Equilibrium pressure values were noted, when xylem water became visible on the cut end of the petiole, which was observed through a binocular microscope.

2.2. Remote sensing data acquisition

Thermal camera Tau 2 (FLIR, Wilsonville, USA) encompassing a single 7.5–13.5 μm broadband channel with 19 mm focal length was mounted on a quadcopter UAV (Matrice 100 DJI, Shenzhen, China) to collect *LST* on 2, 12, 19 and 24 July 2018, and 10 and 26 July 2019, between 10:00 to 16:00 local time at approximately 30-minute intervals, determined by battery capacity and recharging speed (Table 1). The UAV was flown 60 m above ground level after a series of test flights to optimize fine spatial and temporal resolution, at a speed of 5.8 m s⁻¹ and controlled by Pix4D software on a mobile device. The thermal data were obtained and saved as video, and images were extracted from the video frame by ThermoViewer (ThermalCapture, Wilnsdorf, Germany; ver. 2.1.7) and mosaicked by Agisoft Metashape (ver. 1.6.4; Agisoft LLC, St. Petersburg, Russia). Four plates with shades from white to black were scanned before and after each flight by the thermal sensor and temperatures were measured by a hand-held infrared thermometer (Optris MS LT, Optris, Berlin, Germany) for radiometric calibration. Every day before the first UAV flight, the panels were placed on the ground for approximately 30 min to stabilize the temperature to an equilibrium status. An RGB camera Zenmuse X3 was also concurrently used and these images were processed by Pix4Dmapper (Pix4D S.A., Prilly, Switzerland; version 4.2.27) with the “Ag RGB” template. Digital elevation (DEM) and surface models (DSM) were also produced from RGB image processing. All UAV mosaics were geo-referenced and collocated by four to six ground control points placed at the corners of the study area, and resampled to 6-cm spatial resolution. Furthermore, TSEB-PT, originally developed for satellite thermal data, requires certain spatialization of the input data in order to partition the energy fluxes from mixed pixels to canopy and soil components (Norman et al., 1995). For UAV data typically obtained at different and very fine spatial resolution (e.g., a few cm or less), the user needs to resample the original UAV images to run TSEB-PT (Nieto et al., 2019; Xia et al., 2016); however, the effect of spatial resolution on the TSEB-PT canopy and soil partitions of energy fluxes remains unclear. Optimal spatial resolution also minimizes information redundancy and computational resources. Therefore, the UAV images were resampled by averaging to 0.1, 0.5, 1, and 2–24 m (with 2-m increments) to explore the performance of TSEB-PT modelling at different spatial resolutions, and the spatial resolution with the most optimal performance would be used for further analysis.

In addition to the retrieval of thermal and RGB images, a parallel UAV (Matrice 100 DJI, Shenzhen, China) flight campaign with mounted RedEdge (Micasense, Seattle, USA) camera collected multispectral imagery at blue, green, red, red edge and near infrared bands. Details regarding the multispectral data collection are described in Peng et al. (2021a).

Table 1

Available land surface temperature (*LST*) datasets. DAE means days after emergence of the potato (22 May 2018 and 3 June 2019).

Year	Date	10:00	10:30	11:00	11:30	12:00	12:30	13:00	13:30	14:00	14:30	15:00	15:30
2018	02 July (DAE41)		X		X	X	X	X	X	X	X	X	
	12 July (DAE51)		X	X	X	X			X			X	
	19 July (DAE58)	X	X	X	X	X	X	X	X				
	24 July (DAE63)						X			X			
2019	10 July (DAE37)			X					X			X	
	26 July (DAE53)									X	X	X	X

2.3. Modelling evapotranspiration by two-source energy balance

Evapotranspiration was estimated for each flight (Table 1) using TSEB-PT. The “series” over “parallel” version of TSEB was employed in this work as it was expected that the canopy and the soil interact with each other with heat and water exchange, especially under dense-canopy conditions (Nieto et al., 2019).

The model considers that *Rn* equals the sum of *H*, *LE* and *G* (Eq. (1)) and thus neglects heat advection and other fluxes such as heat storage by the canopy layer. *Rn* and the turbulent fluxes are further partitioned between canopy and soil (Eqs. 2–5):

$$R_n = H + LE + G \tag{1}$$

$$R_{nC} = H_C + LE_C \tag{2}$$

$$R_{nS} = H_S + LE_S + G \tag{3}$$

$$H = H_C + H_S \tag{4}$$

$$LE = LE_C + LE_S \tag{5}$$

where subscripts “C” and “S” denote canopy and soil, respectively.

In Eqs. 1–5, *Rn* and *H* can be estimated for canopy and soil by combining multispectral and thermal data with meteorological forcing in a series of equations, as explained below, and *LE* is calculated as the residual of Eqs. 1–5.

The *LST* images containing mixed pixels were partitioned to canopy (*T_C*) and soil (*T_S*) temperature using a weighted mean of emitted blackbody radiance:

$$\sigma T_{rad}^4(\theta_o) = f_C(\theta_o)\sigma T_C^4 + [1 - f_C(\theta_o)]\sigma T_S^4 \tag{6}$$

where *T_{rad}*⁴(*θ_o*) is radiometric temperature, and it is mixed (canopy and soil) *LST* in this paper, *σ* is the Stefan-Boltzman constant (5.67037 × 10⁻⁸ W m⁻² K⁻⁴), *f_C*(*θ_o*) = 1 - exp(-*κ_{be}Ω(θ_o)LAI*) is the fraction of vegetation observed by the thermal sensor looking at *θ_o* view (observation) zenith angle with *κ_{be}* beam extinction coefficient and *Ω(θ_o)* canopy clumping index. *κ_{be}* is given as (Campbell and Norman, 2012) *k_{be}* = $\frac{\sqrt{x^2 + \tan^2 \theta_s}}{x + 1.774(x + 1.182)^{-0.733}}$, where *x* is the ratio of average projected areas of canopy elements on horizontal and vertical surfaces and it is set to 2.085 for potato according to Campbell and Norman (2012), and *θ_s* is sun zenith angle at the time of the flights, calculated by the “Zenith” function from the R package “GeoLight” (Lisovski et al., 2015) given latitude, longitude and UAV flight time in UTC format. *Ω(θ_o)* is calculated as: $\Omega(\theta_o) = \frac{\Omega(0)}{\Omega(0) + [1 - \Omega(0)]e^{-2.2\theta_o^{3.8} - 0.46D_{hw}}}$, where *D_{hw}* is the ratio of vegetation height to width, which was set as 1.25 according to field observation, and *Ω(0)* is the clumping factor when the canopy is viewed at nadir and is given as $\Omega(0) = \frac{-\ln[f_C e^{-k_{be}LAI} + (1-f_C)]}{k_{be}LAI}$, where *f_C* is the fraction of vegetation canopy cover (Kustas and Norman, 1999).

The *T_C* and *T_S* from Eq. (6) can be used to estimate *H_C* and *H_S*:

$$H_C = \rho C_p \frac{T_C - T_{AC}}{r_x} \tag{7}$$

$$H_S = \rho C_p \frac{T_S - T_{AC}}{r_S} \quad (8)$$

where H_C and H_S are sensible heat fluxes of canopy and soil, respectively. r_X and r_S are, respectively, the canopy and soil resistances to heat transport, ρ is air density and C_p is the heat capacity of air. T_{AC} is the aerodynamic temperature (air temperature at the canopy source-sink height) calculated by temperatures and resistances:

$$T_{AC} = \frac{\frac{T_A}{r_A} + \frac{T_S}{r_S} + \frac{T_C}{r_X}}{\frac{1}{r_A} + \frac{1}{r_S} + \frac{1}{r_X}} \quad (9)$$

where T_A is air temperature measured by the meteorological station, r_A is the surface aerodynamic resistance to heat transport. The equations for r_A , r_X and r_S are listed in Appendix A and can be found in Kustas et al. (1999).

Since only $T_{rad}(\theta_o)$ in Eq. (4) can be obtained from the *LST* images and both of T_C and T_S are unknown, Norman et al. (1995) described an iterative process to derive these temperatures, using an initial guess of T_C and consequent estimation of canopy latent heat flux based on the Priestley-Taylor equation:

$$LE_C = \alpha_{PT} f_g \frac{\Delta}{\Delta + \gamma} R_{nc} \quad (10)$$

where α_{PT} is the Priestley-Taylor coefficient initially set to its original value of 1.26, f_g is fraction of *LAI* that is green and thus photosynthetically active (defined as 1 in this work observing that the whole potato canopy was green during this growing period in July), Δ is the slope of saturation vapor pressure with temperature and γ is the psychrometric constant.

At this stage, the initial LE_S estimate is likely to yield negative-unrealistic values at daytime indicating dew condensation at the soil surface, which is unlikely during daytime. TSEB-PT then iteratively reduces α_{PT} in Eq. (10) and re-computes all temperatures and fluxes until realistic LE_S and LE_C are obtained (i.e. null or positive). Further details of the iterative process are shown in Appendix B. Noteworthy is that R_n for canopy (R_{nc}) and soil (R_{ns}) are based on meteorological and remote sensing data (thermal and multispectral) and both can be divided into longwave and shortwave parts. The calculation are listed in Eqs. C1-8 based on Campbell and Norman (2012). The other equations for radiation calculations are listed in Appendix C.

The calculated LE_S and LE_C were further converted to E and Tr , respectively, and LE was calculated as the sum of LE_S and LE_C and was further converted to ET . More detailed information on TSEB-PT can be found in Norman et al. (1995), Kustas and Norman (1999), and Nieto et al. (2019), and the programming code is available online at <https://github.com/hectornieto/pyTSEB> (<https://doi.org/10.5281/zenodo.594732>).

TSEB-PT returns instantaneous canopy and soil fluxes at each UAV flight time. Assuming that LE is consistently proportional to irradiance (Cammalleri et al., 2014; Nassar et al., 2021), daily LE was extrapolated by multiplying the instantaneous LE (at or near to noon) with the ratio of mean daily solar irradiance to instantaneous irradiance at the UAV flight time, and then converted to daily ET .

The biophysical parameters needed to run TSEB-PT were obtained as follows. f_C used as a proxy for canopy clumpiness was derived by first creating an RGB-based vegetation binary mask image at 2-cm spatial resolution from the greenness index (GI , $2 \times$ green–red–blue). A value of 1 in the mask was assigned when the GI value was above a threshold determined by visual interpretation, and 0 otherwise (Zhou et al., 2018; Peng et al., 2021a). Then f_C at the *LST* imagery spatial resolution (6 cm) was obtained by average aggregating the binary mask. The clumping index ($\Omega(\theta_s)$) used for R_n estimation was calculated assuming potato is a row crop with row direction set at 330° (see Fig. 2; Colaizzi et al., 2012; Parry et al., 2019) and its calculation is shown in Appendix B1 from Nieto et al. (2019). The effective leaf width was 0.05 m as an observed mean size of the potato leaflets. The height of the canopy (h_C) was

calculated as a difference between instantaneous RGB digital surface and elevation models calculated before plant emergence. Finally, *LAI* was calculated according to Campbell and Norman (2012):

$$LAI = -2 \cos \theta_s \ln(1 - f_{ipar}) \quad (11)$$

where f_{ipar} is the fraction of intercepted photosynthetically active radiation calculated by a power model $f_{ipar} = a + bRVI^c$ where RVI is the ratio vegetation index, (ratio of reflectance in the near-infra red (NIR) to the red spectrum), and a , b and c are local empirical coefficients derived with the iterative procedure of Christensen and Goudriaan (1993). The reflectance data were obtained by a RedEdge camera mounted on UAV in a parallel flight campaign (Peng et al., 2021a).

2.4. Calibrating sap flow measurements against soil water balance

The 10-minute intervals sap flow measurements were quality controlled as prescribed in the equipment manual (Dynamax, Houston, Texas, USA) and gap-filled by linear interpolation. Sap flow sensors measure the xylem water transport and hence Tr , in unit of $ml\ h^{-1}$. The method, however, provides widely variable values between shoot due to different size and exposure of the selected shoots and a method is needed to scale the values from the individual shoots to express them in $mm\ h^{-1}$ and be able to compare the reading to the TSEB-PT outputs.

Sap flow data ($ml\ h^{-1}$) covering exactly the period between two TDR measurements (up to exact time at 10-minute resolutions) were summed (ml) and used to divide the corresponding ET calculated from a standard water balance for the week (mm), that is to say, $ET_{swb} = \Delta SWD + I + P - D$, where ET_{swb} is ET estimated from soil water balance, ΔSWD is the change or increase in soil water deficit, I is irrigation, P is precipitation and D is drainage during a period between two TDR soil water measurements, and we assumed the xylem water transport summed over the same period is proportional to ET_{swb} . Potential ET (ET_p) was calculated with the FAO56 Penman-Monteith equation (Allen et al., 1998) and a mid-season crop coefficient of 1.15. Weeks were selected where the accumulated ET_p was higher than the sum of SWD , irrigation and precipitation ($SWD + I + P$) during the week indicating negligible drainage and hence the water was transported only by ET . Thereby, a ‘calibration constant’ for each sap flow sensor was obtained allowing estimation of 10-minute recording values, which we denote as Tr_{sap} in the unit of $mm\ h^{-1}$ from the sap flow measurements (Razzaghi et al., 2012). It was assumed that ET_{swb} based on soil water measured in the 0–60 cm soil layer was predominantly utilized by the plants for Tr during these periods where the soil was relatively dry. Once a shallow surface layer has become dry, E is limited in coarse sandy soils (Wang, 2015).

2.5. Empirical calculations and statistics

Crop water use efficiency (WUE) was calculated as:

$$WUE = \frac{NPP}{ET_C} \quad (12)$$

where ET_C ($mm\ d^{-1}$) is actual ET modelled by TSEB-PT and NPP ($g\ m^{-2}\ d^{-1}$) is net primary production estimated according to Peng et al. (2021a):

$$NPP = RUE_{opt} I_{par} f_{Tmax} (1 - \mu f_{CI}) \quad (13)$$

where RUE_{opt} is radiation use efficiency optimized to $4.19\ g\ MJ^{-1}$, I_{par} ($MJ\ m^{-2}\ d^{-1}$) is intercepted photosynthetically active radiation and it was calculated by multiplying f_{ipar} with half the measured global radiation, and f_{Tmax} and f_{CI} are environmental constraints for, respectively, daily maximum temperature and cloudiness (expressed by cloudiness index, CI), ranging from 0 to 1 and aiming to adjust plant production for abiotic factors and μ is a constant (0.46). The equations for f_{Tmax} and f_{CI} calculation are shown in Table 4 in Peng et al. (2021a). Daily irrigation requirement (IR) was calculated as:

$$IR = \frac{ET_P - ET_C}{I_E} \tag{14}$$

where I_E is irrigation efficiency defined as the ratio of applied volume of water to volume delivered to the surface of the field and set to 0.9 – a value combining sprinkler and gun irrigation applied in this study (Olesen and Plauborg, 1995; Thyssen and Detlefsen, 2006).

The treatment plots were used as the area of interest to extract weighted mean values of modelled Tr and ET , using the “extract” function from the “raster” package (Robert et al., 2012) in R. The modelled Tr was correlated with the sap flow data and the fit evaluated by coefficient of determination (R^2), root mean square error ($RMSE$) and mean bias. The strength of the correlations between g_s and LWP with the modelled Tr were evaluated by R^2 as well.

$$R^2 = \frac{(\sum_{i=1}^n (Mod_i - \bar{Mod})(Obs_i - \bar{Obs}))^2}{\sum_{i=1}^n (Mod_i - \bar{Mod})^2 \sum_{i=1}^n (Obs_i - \bar{Obs})^2} \tag{15}$$

$$RMSE = \sqrt{\frac{\sum_{i=1}^n (Obs_i - Mod_i)^2}{n}} \tag{16}$$

$$Bias = \frac{\sum_{i=1}^n (Obs_i - Mod_i)}{n} \tag{17}$$

where Obs_i and Mod_i are observed and modelled values, respectively, and \bar{Obs} and \bar{Mod} are corresponding mean observed and modelled values, n is the total number of observations. Since the sap flow data were processed for unit conversion based on the soil water balance, the comparison was also conducted with the modelled ET in order to assess how well the integrative process of Tr and E is reflected by the modelled ET .

A spatial sensitivity test was conducted to investigate the effect of data spatial resolution on the performance of the TSEB-PT by resampling the input data of LST , f_C , LAI , and h_C from the original 0.06 to 0.1, 0.5 and 1 m, and further from 2 to 24 m (with 2-m increments) and modelled variables (Tr and ET) were compared with the measured ones (sap flow measurements) using R^2 and $RMSE$.

3. Results

3.1. Model validation and effect of spatial resolution

The spatial sensitivity test (linear regression between the Tr estimated from UAV images by TSEB-PT modelling at multiple spatial resolution and from sap flow measurements) showed that the TSEB-PT model performance varied in relation to the spatial resolution of the input data (0.06 to 24 m; Fig. 3). From 0.06 to 10 m, R^2 and $RMSE$ values ranged from 0.60 to 0.80 and 0.055–0.075 $mm\ h^{-1}$, respectively. With highest R^2 and lowest $RMSE$, 1 m was the optimal spatial resolution for modelling Tr and ET using TSEB-PT with UAV data. From 12 m resolution, the model accuracy showed oscillating variation, indicating unstable modelling performance between 12 and 24 m resolutions. Spatial resolutions finer than 1 m (0.06, 0.1 and 0.5 m) were also investigated and here the model accuracy was slightly lower than that at 1 m, according to R^2 and $RMSE$ values (Fig. 3). The linear regression analyses were also conducted for ET (Fig. S2 in the Supplementary material), and these results also identified 1 m as the optimal spatial resolution for energy flux modelling with TSEB-PT and UAV thermal data.

The correlations between Tr (and ET) modelled by TSEB-PT based on the UAV data at 1-m spatial resolution vs. the sap flow measurements are illustrated in Fig. 4. The Tr was in close agreement with the sap flow values (regression equation $y = x - 0.007$), with a high R^2 value (0.80), and low $RMSE$ (0.055 $mm\ h^{-1}$) and bias ($-0.01\ mm\ h^{-1}$; Fig. 4 A). However, TSEB-PT showed a slight underestimation for the low values (mainly in the low irrigation treatment), which indicates difficulties to accurately estimate the low levels of Tr observed by the sap flow equipment under drought (e.g., 0.02 $mm\ h^{-1}$). In contrast, the modelled ET was overall 20% higher than the sap flow values, with low R^2 (0.56) and high $RMSE$ (0.15 $mm\ h^{-1}$) and bias (0.09 $mm\ h^{-1}$; Fig. 4 B).

3.2. Diurnal variation of evapotranspiration

The diurnal dynamics of the modelled Tr and ET of potato based on 1 m spatial resolution UAV LST data under full irrigation conditions are shown in Fig. 5. Less precipitation (11.2 mm, see Table S1 in the Supplementary material) during the UAV campaigns in 2018 (02–26 July)

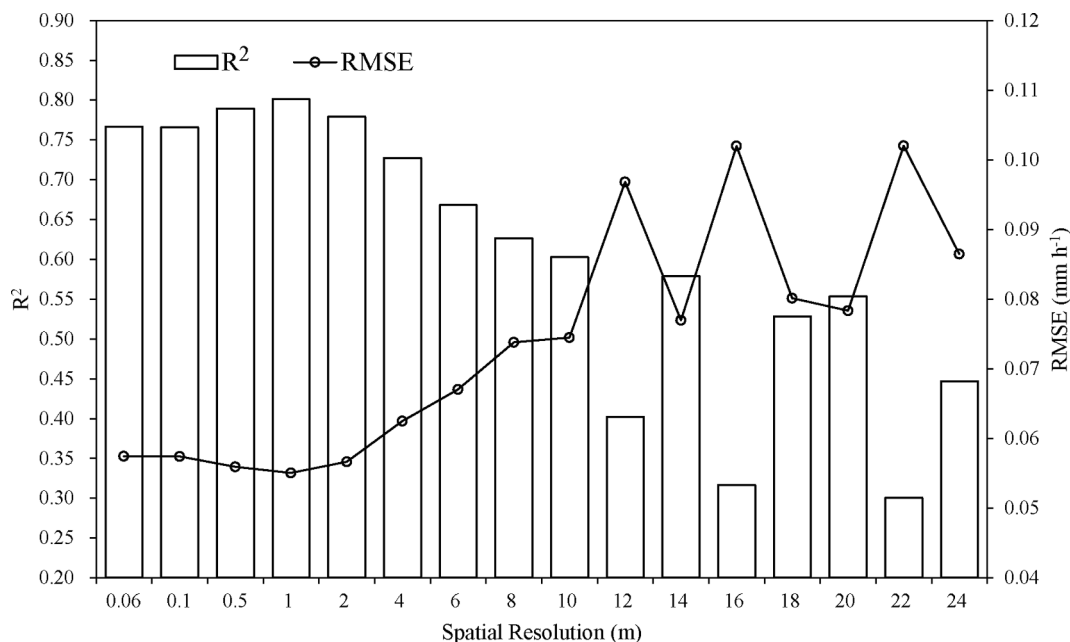


Fig. 3. Effect of spatial resolution on the performance of the two-source energy balance model based on the Priestley-Taylor equation (TSEB-PT) in this study. The determination of coefficient (R^2) and root mean square error ($RMSE$) values were obtained from the comparison between the transpiration (Tr) estimated from unmanned aerial vehicle (UAV) images by TSEB-PT at multiple spatial resolution and from calibrated sap flow measurements.

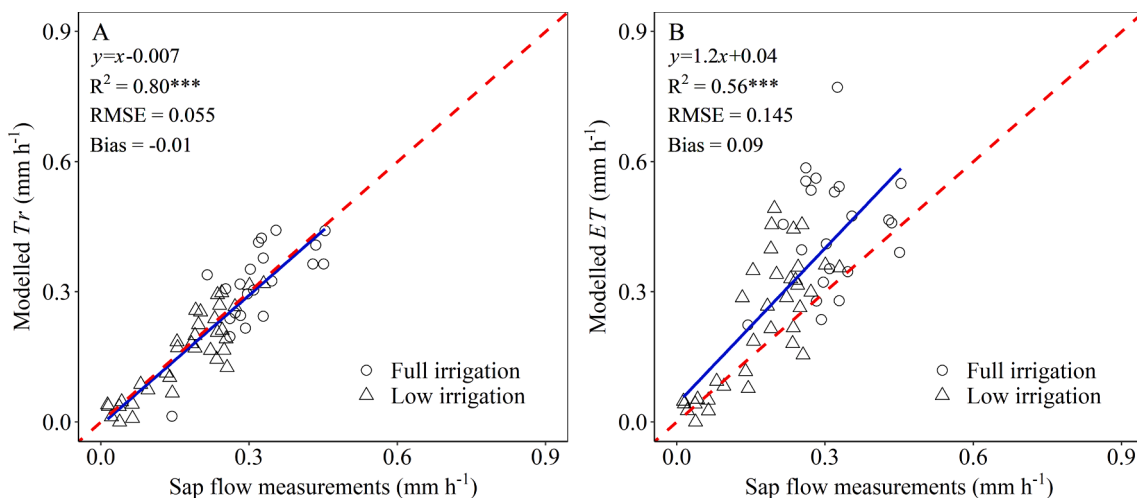


Fig. 4. Relationship between sap flow measurements and modelled transpiration (Tr , A) and evapotranspiration (ET , B). The dotted line is the 1:1 line. Each dot represents a weighted mean value, modelled from land surface temperature images by the two-source energy balance model based on the Priestley-Taylor equation (TSEB-PT) at 1 m spatial resolution recorded by unmanned aerial vehicles (UAVs) for all available flights in the full (circles) and low (triangles) irrigation treatments (see Table 1). Linear equation for the fits are also presented on each plot. *** denotes significant at $p < 0.001$ level.

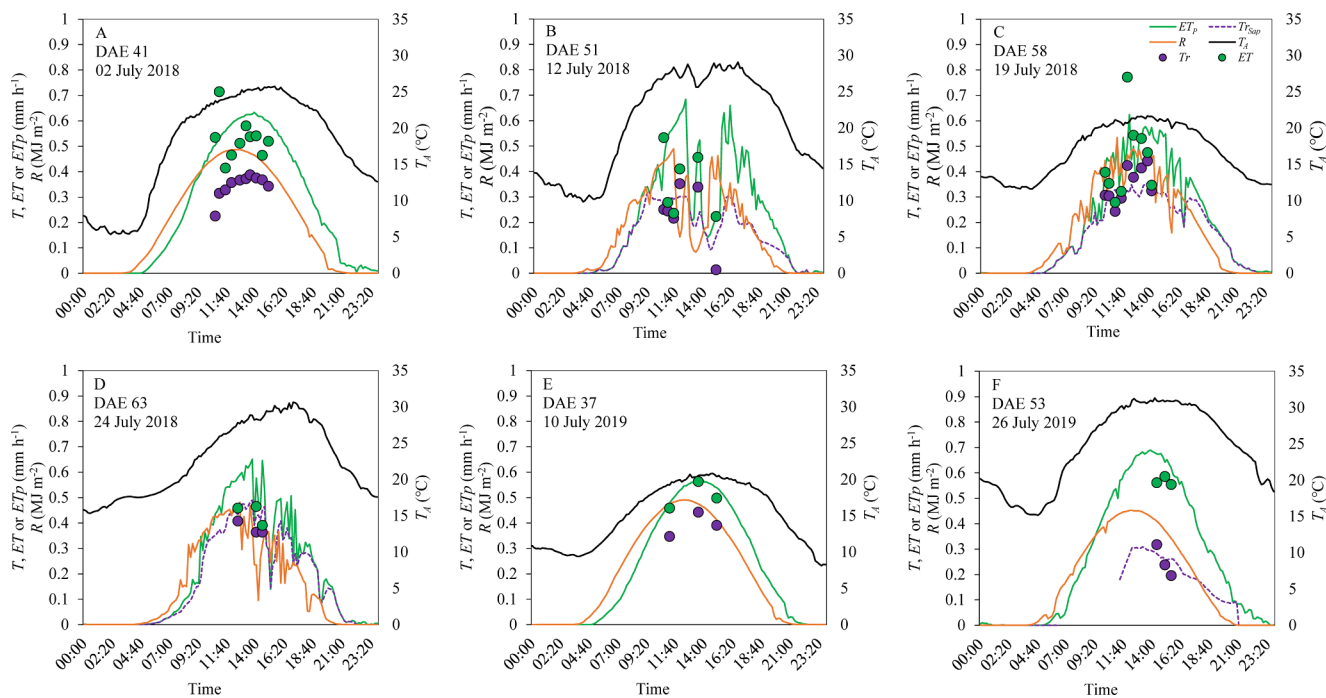


Fig. 5. Full irrigation two-source energy balance model estimates based on the Priestley-Taylor equation (TSEB-PT) of actual transpiration (Tr , purple circles) and evapotranspiration (ET , green circles) modelled from unmanned aerial vehicle (UAV) land surface temperature (LST) data at 1 m spatial resolution, and Tr_{Sap} data (Tr , dotted purple line). The 10-minute intervals variation in potential evapotranspiration (ET_p) of potato from the fully irrigated plots is also shown as a solid green line. On 2 July 2018 and 10 July 2019, sap flow equipment was not installed yet, hence no data (see Section 2.1). The air temperature (T_A) and global radiation (R) are shown in the figure as well. (For interpretation of the references to colour in this figure legend, the reader is referred to the web version of this article.)

contributed to drought stress, compared to the same period in 2019 (41.1 mm). The estimated Tr followed Tr_{Sap} and the diurnal variations of Tr and ET followed the pattern of ET_p for the fully irrigated plot. In most cases, the soil E flux contributed notably to ET (especially, on 2 July 2018 and 26 July 2019; Fig. 5). Moreover, at certain instances (e.g., 11:00 on 2 July and 12:00 on 19 July in 2018), modelled ET values were higher than ET_p due to high Tr and E . One reason for this overestimation is overestimated modelled Tr (e.g., being 0.12 mm h^{-1} higher than the sap flow value at 12:00 on 19 July 2018) derived from relatively low LST compared to other times on the same day. Another likely reason would be the ample water supply from the irrigation and the high-energy input

from the solar radiation (at noon).

Under low irrigation, the modelled Tr at 1 m spatial resolution closely followed the Tr_{Sap} , and both were overall close to ET due to the low E (Fig. 6). On a few occasions (e.g., 19 July 2018 and 10 July 2019), drought was alleviated by a small amount of precipitation and dewfall (a day or two earlier), which also lowered temperature (see precipitation data in Table S1 and diurnal variation of dew point in Fig. S1 from Supplementary material). The Tr_{Sap} from the low irrigation on 24 July 2018 did not follow the dynamics of ET_p and were close to zero. For the other days, Tr_{Sap} followed the dynamics of ET_p during the early morning, but soon started to deviate with an offset due to root zone soil water

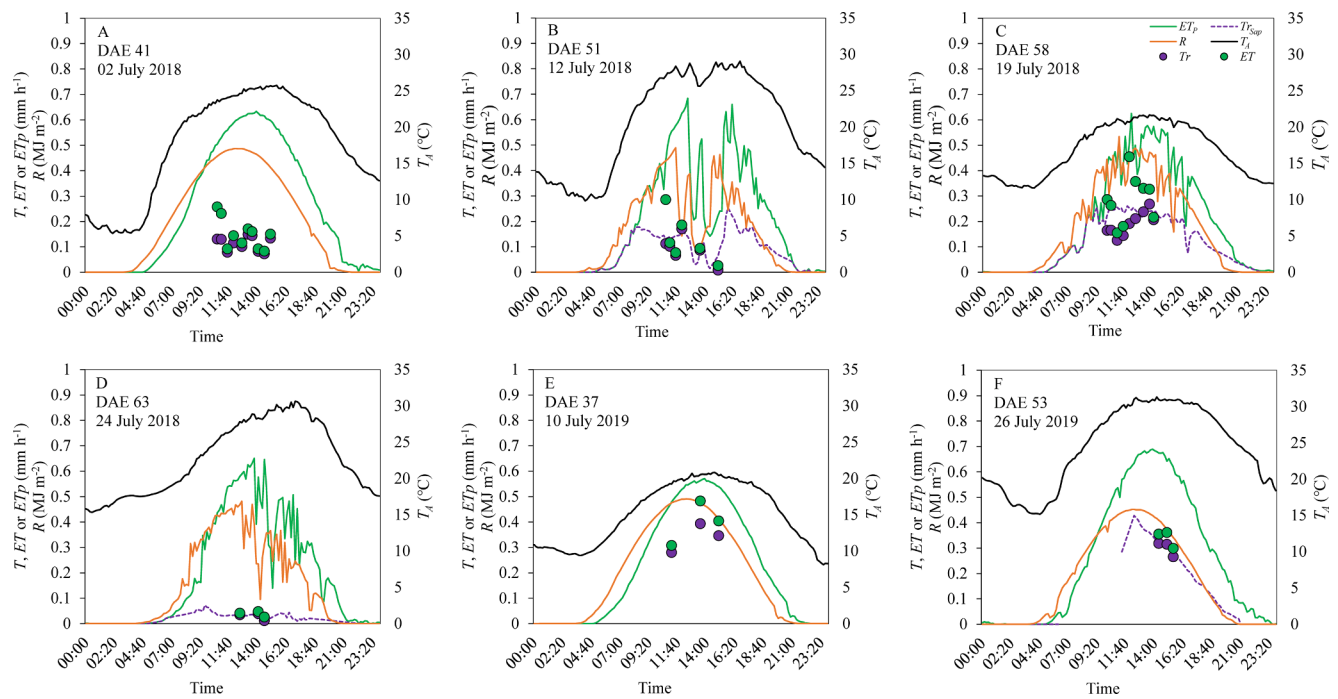


Fig. 6. Low irrigation two-source energy balance model estimates based on the Priestley-Taylor equation (TSEB-PT) of actual transpiration (T_r , purple circles) and evapotranspiration (ET , green circles) modelled from unmanned aerial vehicle (UAV) land surface temperature (LST) data at 1 m spatial resolution, and Tr_{sap} data (Tr , dotted purple line). The 10-minute intervals variation in potential evapotranspiration (ET_p) of potato from the fully irrigated plots is also shown as a solid green line. On 2 July 2018 and 10 July 2019, the sap flow equipment was not installed yet, hence no data (see Section 2.1). The air temperature (T_A) and global radiation (R) are shown in the figure as well. (For interpretation of the references to colour in this figure legend, the reader is referred to the web version of this article.)

depletion.

3.3. Correlation of modelled transpiration with leaf parameters

LWP was significantly, positively and linearly related to T_r ($R^2 = 0.81$), and g_s was significantly, positively, and exponentially related to T_r ($R^2 = 0.74$; Fig. 7). The relationships also showed good discrimination between treatments, with overall lower values for low irrigation and vice versa.

It can be seen on Fig. 7B that a cluster of points opposing the exponential trend as these data were from the low irrigation treatment on 19th July 2018 at 12:00–14:00, when the drought stress was not high compared to the other days due to the relatively low T_A and R_n (Fig. 6),

hence g_s was considerable. However, in the low irrigation plot, the canopy cover was not as high as the full irrigation plot, which likely exposed the soil (see Fig. 2 B); thus it was likely that part of the water in the soil obtained from the irrigation (17th July 2018, see Supplementary material) and dewfall was evaporated and T_r was not very high.

3.4. Water use efficiency and irrigation demand

A CASA model with radiation use efficiency depending on maximum daily temperature but not soil or plant water status (Peng et al., 2021a) was used together with the TSEB-PT ET estimates. This allowed visualization of the spatio-temporal variation of ET , NPP , WUE and IR , as illustrated in Fig. 8 for two plots with contrasting irrigation treatments.

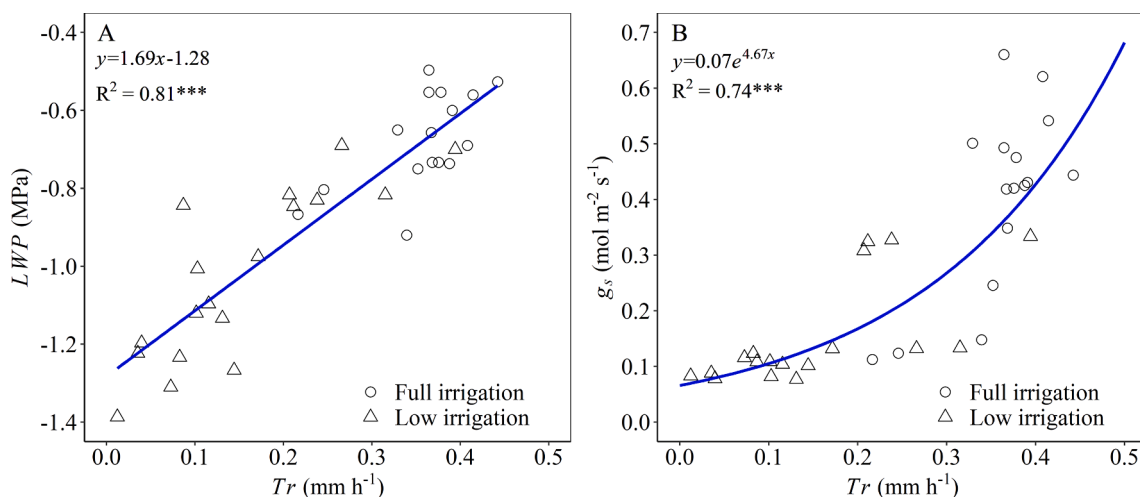


Fig. 7. Relationship between (A) leaf water potential (LWP) or (B) stomatal conductance (g_s) and modelled transpiration (T_r) for the potato plots on specific measurement days in July 2018 and 2019. The solid line shows regression fit as described by the equations. *** denotes the significant level ($p < 0.001$).

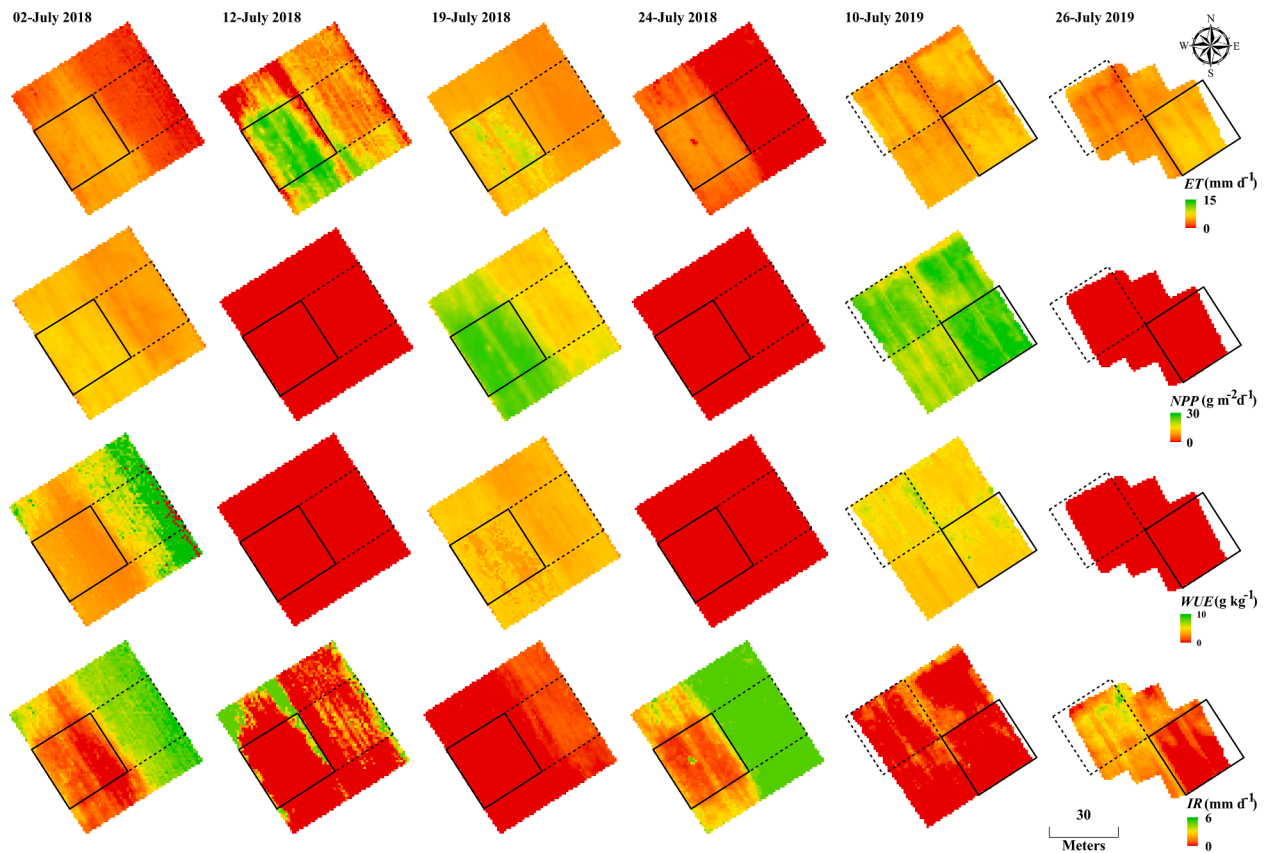


Fig. 8. Maps of evapotranspiration (ET), net primary production (NPP), water use efficiency (WUE , $\text{g DM kg H}_2\text{O}^{-1}$), ratio of NPP and ET , and irrigation requirement (IR) estimated for 2, 12, 19, and 24 July 2018 and 10 and 26 July 2019 for the treatment plots with potatoes. The squares displayed on the figures delineate the location of the irrigation treatment (solid squares indicate full irrigation and dashed squares indicate low irrigation.).

The spatial distribution of ET and NPP corresponded well with each other, showing higher ET and NPP with full irrigation and *vice versa* in most of the cases. However, there were exceptions when there was heat stress. For example, on 12 and 24 July 2018 and 26 July 2019, the daily NPP was zero even for the fully irrigated plot due to heat stress halting the growth (daily maximum air temperature exceeded 29°C according to Peng et al. (2021a)). Accordingly, WUE was low and independent of ET level. On other days its spatial distribution depended on the drought conditions. On 19 July 2018 and 10 July 2019 the spatial pattern of WUE followed that of NPP and ET as there was little or no drought stress. However, on 02 July 2018, an increase of WUE in the drought stressed plot was revealed despite NPP being lower than in the fully irrigated plot. The spatial patterns of IR (determined by Eq. (14)) corresponded inversely to ET (Fig. 8), showing a close relationship between them. According to the distributions of IR , there was very little or no need for additional irrigation in the fully irrigated plot, even under widespread drought conditions (24 July 2018 and 26 July 2019), whereas for the low irrigation plot, the calculated IR ranged from 3 to 6 mm d^{-1} , which corresponded well with the real irrigation amounts applied to the fully irrigated plot (around 30 mm per week, see Table S1 in Supplementary material) indicating reliability of the IR calculation.

4. Discussion

4.1. Modelling evapotranspiration with a two-source energy balance model

The TSEB-PT modelled Tr at 1-m spatial resolution was in excellent agreement with the sap flow measurements (Fig. 4A), which provides the evidence that the assumption that the majority part of SWC (used for sap flow measurements calibration) detected by TDR sensor in the 0–60

cm soil layer was predominantly utilized by the plants for Tr and not by the soil for E . The reason is that in coarse sandy soil, only the water retained in the few centimeter surface layer will be evaporated and water below surface layer is either leached to deeper layer or used by plant Tr (Wang, 2015); under drought conditions, this part E can be neglected in the soil water balance model used for sap flow measurements calibration. However, this does not mean that there was no E in the field since the deviation of ET compared to Tr (Fig. 4) showed there was notable E . It is because if there was extra water source, i.e. from irrigation, the water kept by the surface soil layer would be evaporated soon under drought conditions and the weekly measured TDR sensors were likely less sensitive to this water movement. Furthermore, modelled Tr correlated closely to field measurements of LWP and g_s (Fig. 7). The relationship between g_s and Tr was described with an exponential regression model (performing more accurately than linear), likely due to the influence of vapor pressure deficit (VPD) on both Tr rate and g_s : $Tr \sim g_s \times VPD$ with g_s being also sensitive to VPD (Grossiord et al., 2020; Leuning et al., 1995; Zhang et al., 2022). The high ET in the fully irrigated area indicated that the crops transported water from the soil towards the leaves and stomata, inducing a cooling effect that was most pronounced at noon (Fig. 8), alleviating drought stress, and at the same time lessening otherwise severe and confounded heat stress (Blum, 2009; Yoo et al., 2009). The low ET in the low irrigation plot (almost 0 at noon, especially on 12 and 24 July 2018; Fig. 6) showed that the plants closed the stomata to reduce water loss and avoid cavitation in the xylem, but at the expense of inflicted heat stress (Teskey et al., 2015) that may severely limit NPP in potatoes even at moderate temperatures (Peng et al., 2021a; Zhou et al., 2017). Furthermore, E under low irrigation was limited (especially on drought days) due to the combined effects of limited SWC and lack of water transport in the sandy soil's surface layer. Therefore, most of the irradiance transferred to the soil is

converted into sensible heat flux, which is the reason why *LST* of the soil for the low irrigation area was high – typically above 45°C from 12:00–15:00 versus around 25°C in the fully irrigated. After wetting by rain or irrigation, this top layer is characterized by fast drying that breaks the hydraulic contact with the subsoil, thus reducing *E* (Wang, 2015). However, under full irrigation and except for a few points with low ET_p , there was considerable *E* (Fig. 5) even under high canopy cover (more than 90%; Fig. 2 B). This is likely due to small patches with bare soil exposed to sunlight (e.g., sampled place, furrow, machinery track), which were wet due to irrigation and thus contributing to soil latent heat flux and *E*. The plant canopy is a porous medium (not solid sheets, but loosely stacked leaf layers) with small gaps from which radiation can penetrate as un-intercepted direct and diffuse irradiance (Pallardy, 2008) but can also be transmitted and scattered by the leaves (Fitter and Hay, 2002). For the same field experiment, the fraction of intercepted photosynthetically active radiation (f_{par} ; visible spectrum) estimated from UAV multispectral data from the full irrigation plot reached 0.8–0.98 in July 2018 and 0.88–0.91 in 2019 (Peng et al., 2021a). This result indicated that some PAR reached the soil despite high canopy cover. For solar radiation other than PAR (infrared from 700 to 4000 nm accounting for slightly more than 50% of the incoming radiation; Bhatia, 2014), a larger part is transmitted through the canopy to the ground surface due to the spectral/structural properties of leaves and stems (Campbell and Norman, 2012), which may contribute to *E* as well.

On the other hand, part of *E* may also originate from canopy dew and intercepted irrigation water, e.g., on 2 and 12 July 2018, in the low irrigation plot, the water source for the notable *ET* at 10:30 was likely from dew (Fig. S1 & Fig. 6). Fig.S1 shows that during morning (00:00–07:00) on all six days, the relative humidity was high (close to 100%) and the air temperature was very close to the dew point, which indicated that dewfall occurred. This phenomenon (enhanced *E* from dewfall on both leaves and soil) points to a limitation of TSEB-PT (and other comparable energy-balance models) in its inability to account for this additional heat/water source. It was expected that the sap flow measurements calibrated against changes in *SWC* would correlate better with modelled *ET* than *Tr* and part of this discrepancy (Fig. 6) may be explained by the inability of the model to take proper account of wetting of the leaves and soil surface by dew. The TSEB-PT model was originally developed and tested for semiarid and subhumid areas, which are relatively different compared to higher latitude areas e.g. Scandinavian countries (Kustas and Norman, 1999; Norman et al., 1995). This indicated that for the application of the TSEB-PT model in higher latitude areas, the model should be modified for the local environmental conditions e.g. by including an interception reservoir to achieve higher model accuracy.

Low *Tr* and *ET* values under full irrigation do not necessarily imply drought stress (e.g., 15:00 on 12 July 2018; Fig. 5), but might be a consequence of low irradiance due to clouds, aerosols and atmospheric water vapor, all of which reduce atmospheric transmittance (Lee et al., 2009; Li et al., 2017; Pérez and Coma, 2018). The good agreement between the modelled *Tr* and the sap flow data revealed little effect of such conditions on the results since clouds or aerosol lowered ET_p and sap flow, but also *LST*, resulting in proportionally lower *Tr* and *ET* values modelled by TSEB-PT. Similar results were reported by Hoffmann et al. (2016). However, it should be emphasized that *LST* data should ideally be obtained under conditions of stable irradiance without scattered clouds, as the cloudiness can lead to rapidly changing irradiance, hence a large, induced variability of *LST* during a UAV flight.

Regarding the daily *LE* and *ET* calculations, it was assumed that the ratio of *LE* over irradiance is preserved during daytime. This simple approach has been evaluated in previous studies showing its adequate performance with instantaneous *LE* estimations around noon (Cammalleri et al., 2014). However it is a not a perfect method to capture the diurnal variation in severely stressed crops (Antoniuk et al., 2021) and additional uncertainties raise when this method is applied later in the afternoon (Nassar et al., 2021).

4.2. The use of UAV data for modelling evapotranspiration with high spatio-temporal resolution

Thermal data obtained by UAVs appear to have potential for application and validation of land-surface models at high spatio-temporal resolution with their merits over heterogeneous landscapes yet to be revealed. Spatial resolutions finer than 1 m, i.e., 0.06, 0.1 and 0.5 m, were investigated and the model accuracy was slightly lower (Fig. 3). The likely reason being that, as with many other energy flux models, TSEB-PT radiation and turbulent transport simulations require some degree of spatial aggregation in order to comply with the assumption of effective radiative transfer and turbulent mixing (Burchard-Levine et al., 2021; Nieto et al., 2019). Exploring the spatial resolution effects on the TSEB-PT modelling through images acquired at different UAV flight altitudes is difficult as different flight times sense variable *LST* over the flights, resulting in non-comparable data. In addition, higher altitudes (>100 m) are associated with larger atmospheric attenuation due to a thicker water vapor layer to which *LST* and *ET* are very sensitive. Therefore, *LST* and *ET* between flights at different altitudes would not only be affected by the spatial resolution (e.g., the model sensitivity to the different input spatial resolution), but also to the uncertainties in input retrieval (e.g. the thermal images atmospheric corrections). One meter resolution was optimal for the performance of TSEB-PT and coarser resolutions, especially larger than 10 m, downgraded the accuracy significantly. Therefore, coarse resolution studies typically applied in large-scale agronomic, hydrological and environmental research should consider this uncertainty when coupling UAV thermal data over agricultural fields for *ET* calculation. Wang et al. (2019) found similar results for *ET* modelled by the Priestley-Taylor Jet Propulsion Laboratory model against eddy covariance measurements. Several analyses of the effect from the spatial resolution on the *ET* modelling using satellite data for large fields showed that important spatial patterns would be lost at coarser spatial resolution (Li et al., 2008; Li et al., 2021). Therefore, the utilization of UAV data could be an efficient and functional support for satellite-based *LST* analyses.

The high temporal resolution is another important merit of UAV systems. Previous studies using a diurnal timescale revealed the ratio of actual to potential *ET* being higher in the morning, decreasing at noon hours and ‘recovering’ in the afternoon, referred to as hysteresis effect (Antoniuk et al., 2021). In this study (Figs. 5 and 6), similar results were found especially for the full-irrigated area with ample water supply (e.g., 12 July 2018). The agreement between TSEB-PT modelled *Tr* and sap flow measurements during morning hours on the 12, 19 and 24 July 2018 (Figs. 5 and 6) should be noted. Both initially followed ET_p but started to deviate earlier in the drought stressed plants (at a level around 0.2 mm h⁻¹ or less) than in the fully irrigated (at a level around 0.3 mm h⁻¹). Drought stressed plants are capable of transpiring at potential rate in the early morning hours, as they rehydrate during night and use water stored in plant tissue (Andersen et al., 1991) for *Tr*, which however quickly cease when the difference between *Tr* and root water uptake leads to tissue dehydration (Jensen et al., 1993; Katerji et al., 1986). This diurnal temporal resolution of the UAV data offers the opportunity to explore the variation of the heat flux of agricultural fields within a day at hourly resolution, which could promote precision irrigation activities (Fig. 8).

The high spatial resolution of UAV data can also have shortcomings, mainly related to covering larger fields, flight limitations under weather with strong winds and radiometric uncertainty of the thermal microbolometer cameras. Also, integrated within smart-farming solutions, UAV systems/services appear out of reach, e.g., in the Mediterranean region, where many farming systems utilize satellite data as a decision-support option, due to free access and considerably lower cost. Several studies have conducted relatively reliable modelling of *ET* by TSEB-PT at spatial resolution of 20 to 60 m using Sentinel-2 and -3 images (Bellvert et al., 2020; Guzinski and Nieto, 2019) or Landsat (Knipper et al., 2019) at 30 m spatial resolution. However, for the requirements of practical agronomic operations and precision agriculture targeting reduced and especially deficit irrigation (DI), finer and more precise *LST* data are

needed and this is one of the largest merits of UAV.

LST images collected by thermal cameras mounted on UAVs contain sources of uncertainty, such as the internal non-uniformity correction (NUC) and temperature drift, and environmental factors (e.g., air humidity and surface emissivity property) (Aubrecht et al., 2016; Meier et al., 2011; Mesas-Carrascosa et al., 2018; Olbrycht et al., 2012). These uncertainties affect the quality of the UAV *LST* images, thus special attention (e.g., camera system updating and *LST* data radiometric calibration) should be given to the data collection.

4.3. Drought stress detection and implications for irrigation management

The positive relationship between both *LWP* and g_s with *Tr* coincide with Xue et al. (2021) for tomato cultivated in a climate chamber at different (full/deficit) irrigation and salinity levels. The distribution of low and full irrigation data points in Fig. 7 shows a division at a *Tr* level of approximately 0.28 mm h^{-1} , which corresponds to *LWP* of -0.8 MPa , a threshold value for drought stress that was supported in previous studies (Hsiao and Acevedo, 1975; Taiz and Zeiger, 2010). However, these thresholds depend on both the environmental conditions and the crop development stage (e.g. García-Tejera et al., 2021; Zhang et al., 2022) and need caution for field irrigation scheduling and operation to not induce severe yield losses.

The spatial distribution of the *WUE* indicated that slight but not severe drought stress derived from low irrigation could increase *WUE* (e.g. on 02 July 2018 in Fig. 8). This agrees with Zhang et al. (2022), Liu et al. (2005a, b), and Liu et al. (2006a), who concluded that mild soil water deficit improved *WUE* of potatoes since crop *Tr* was significantly reduced but crop photosynthesis and growth rate were maintained. Besides improving *WUE*, the irrigation strategies other than full irrigation, such as partial root-zone drying (PRD) and DI could help crops to enhance root systems and increase soil nutrient uptake (Kirida et al., 2005; Liu et al., 2006b; Shahnazari et al., 2007). However, in comparison to DI, the applicability of PRD for large-field management is relatively low (except for furrow/ridge crops) and uniform DI is currently more feasible. Compared to the use of soil water balance models in the DI application, which increases risks of yield loss (Trout et al., 2020) due to underestimation of drought stress or reasons like misjudged root depth in all or parts of a field, direct spatio-temporal resolved measurements of actual *ET* (the ratio or difference between actual and potential *ET*, which were demonstrated in this study) could provide new opportunities for regulated DI scheduling with high precision and less risk of yield loss. Specifically for potatoes, reducing irrigation to 70–75% of *ET* during the late stages of growth has shown promising results (Crosby and Wang, 2021; Shahnazari et al., 2007) while many other crops typically are less sensitive to mild drought during their vegetative growth (Steduto et al., 2012). Development of such tools and strategies to increase *WUE* is urgently needed to support global food security in the light of ever-increasing competition for finite water resources worldwide (Steduto et al., 2012). In the current study, the modelled *IR* reflected the modelled *ET* and *NPP* well (Fig. 8), indicating the water need for the stressed plants with low *ET*, hence low *NPP*.

Drought and heat stress are intimately connected, since drought may induce extreme canopy temperatures due to lack of evaporative cooling as shown in this study and elsewhere (Berg et al., 2015), while high temperatures due to its linkage with vapor pressure deficit may induce drought stress (e.g. Lesk et al., 2021; Lobell et al., 2013; Zhang et al., 2022). Therefore, it is intrinsically difficult to single out their individual effects and their interaction on crop growth. Present crop simulations models may not adequately consider a rise of canopy temperature of $20\text{--}25 \text{ }^\circ\text{C}$ above measured air temperature, as seen here, due to drought. This coupling thus remains a gap in understanding present and future climate impacts on crop productivity (Lesk et al., 2021). In our simple approach to distinguish the effects of the two factors, we used a moisture-insensitive data driven *NPP* model (Peng et al., 2021a) in combination with the present TSEB-PT to derive *WUE*, which is a key

factor to consider in water-limited environments. Peng et al. (2021a) firstly quantified the effect from daily maximum air temperature on the potato *NPP* based on statistical analysis of historical data for irrigated potatoes (Table 4 and Fig. 5 A from Peng et al. (2021a)). The *NPP* model takes daily maximum air temperature as one of the inputs, although it may be argued that *LST* would be a better input, which displayed reduced and even halted photosynthesis and growth of potato under prevailing air temperatures for both irrigated and non-irrigated treatments (e.g., 12 and 24 July 2018 and 26 July 2019, Fig. 8) and this is in line with results of Timlin et al. (2006). From a management perspective, this raises the dilemma whether it is worthwhile to irrigate a crop during high temperature periods. The *NPP* model (Peng et al., 2021a) predicts a parabolic decrease of production from an optimum daily maximum temperature of c. $17 \text{ }^\circ\text{C}$ to zero at c. $29 \text{ }^\circ\text{C}$. Thus, raising temperatures above $17 \text{ }^\circ\text{C}$ will almost certainly decrease *WUE* and the profitability of irrigation. Nevertheless, irrigation will help to sustain crop's survival by cooling (Lobell et al., 2008) and decrease production (and possible quality) losses in the indicated temperature range. Adequate water supply may even cool the crop to several degrees below the ambient air temperature (Antoniuk et al., 2021).

The accurate estimation of *ET* (thus drought stress) and *IR* also contributes to the estimation of N deficiency and fertilization amount since drought limits the plant's ability for nutrient uptake, despite these being abundant in the root zone (Dalla Costa et al., 1997; Obidiegwu et al., 2015; Peng et al., 2021b). Therefore, future studies should investigate how well drought and nutrient deficiency stress could be distinguished. Overall, our approach for the *ET* modelling and *IR* calculation have demonstrated the large potential for application to operational irrigation scheduling that seems especially promising for the management of regulated DI and associated water savings.

5. Conclusion

In this paper, the TSEB-PT model was applied using thermal, multi-spectral and RGB images obtained by UAVs to calculate actual *Tr* and *ET* of potato plants grown under contrasting irrigation treatments on a sandy soil, and to quantify drought stress and irrigation requirements. The main findings can be summarized, as follows:

- (i) The TSEB-PT modelled *Tr* corresponded well with measured sap flow and spatial sensitivity test revealed that 1 m was the optimal spatial resolution.
- (ii) Diurnal variation of *Tr* followed the sap flow observations and convincingly revealed the effect of drought on plant *Tr* and *ET*. The results pinpointed the need for surface energy balance models to account for evaporation from the leaf surface from dew and irrigation intercepted water, especially for high latitude areas. The modelled *Tr* was well-correlated to plant physiological parameters *LWP* and g_s .
- (iii) A simple way to distinguish drought and heat stress was presented, which could be helpful for making more informed decisions on management strategies to alleviate these confounded stressors.
- (iv) Precise quantitative irrigation requirements were derived from TSEB-PT. Therefore, the approach has potential for accurate spatio-temporally resolved estimation of plant drought status and *IRs* as required for water saving regulated DI.

CRedit authorship contribution statement

Junxiang Peng: Conceptualization, Methodology, Software, Formal analysis, Data curation, Investigation, Visualization, Writing – original draft. **Hector Nieto:** Methodology, Software, Formal analysis, Investigation, Writing – review & editing. **Mathias Neumann Andersen:** Conceptualization, Methodology, Supervision, Project administration, Funding acquisition, Writing – review & editing. **Kirsten Kørup:**

Methodology, Investigation, Data curation, Supervision, Writing – review & editing. **Rene Larsen:** Investigation, Data curation. **Julien Morel:** Writing – review & editing. **David Parsons:** Writing – review & editing. **Zhenjiang Zhou:** Funding acquisition, Writing – review & editing. **Kiril Manevski:** Methodology, Investigation, Data curation, Supervision, Visualization, Writing – review & editing.

Declaration of Competing Interest

The authors declare that they have no known competing financial interests or personal relationships that could have appeared to influence the work reported in this paper.

Acknowledgement

The authors would like to thank Foulumgård Research Station at Aarhus University for technical support during the field experiments.

Appendix A

The equation for aerodynamic resistance at the surface (r_A) is given as (Norman et al., 1995):

$$r_A = \frac{\left[\ln\left(\frac{z_U-d}{z_M}\right) - \psi_M \right] \left[\ln\left(\frac{z_{T_A}-d}{z_M}\right) - \psi_H \right]}{k^2 U} \tag{A.1}$$

where z_U and z_{T_A} are the heights of wind speed (U , $m\ s^{-1}$) and air temperature (T_A , $^{\circ}C$) measurements respectively, and they are 2 m in this paper. d is the zero-plane displacement height ($d = 0.65\ h_C$, where h_C is canopy height and it was calculated as a difference between instantaneous digital surface and elevation models calculated before plant emergence), z_M is roughness length for momentum transport ($z_M = h_C/8$), k is von Kármán constant (0.41). ψ_M and ψ_H are the adiabatic correction factors for momentum and heat transports and they are given in Brutsaert (2005). These corrections depend on the atmospheric stability, which is described using Obukhov stability length L (m):

$$L = \frac{-u_*^3}{k \left(\frac{g}{T_A}\right) \left(\frac{H}{c_{p\rho}} + \frac{0.61T_A E}{\rho}\right)} \tag{A.2}$$

where g is acceleration of gravity ($9.8\ m\ s^{-2}$), H is sensible heat flux, c_p is heat capacity of air ($J\ kg^{-1}\ K^{-1}$), ρ is air density ($kg\ m^{-3}$), E is evaporation, u_* is friction velocity and it is defined as:

$$u_* = \frac{kU}{\ln\left(\frac{z_U-d}{z_M}\right) - \psi_M\left(\frac{z_U-d}{L}\right) + \psi_M\left(\frac{z_M}{L}\right)} \tag{A.3}$$

In the iterative process of TSEB-PT, the initial value of L was given as infinite ($\frac{z_U-d}{L}$ and $\frac{z_M}{L}$ were therefore 0, i.e. stable conditions), then Eqs. A1-5 were solved and initial r_A was obtained. With the progress of the iterative process, H and E values in Eq. A(4) are updated, thus Eqs. A1-5 are updated as well, and eventually r_A is determined when iterative process finishes. The details for iterative process are shown in Appendix B.

The equation for aerodynamic resistance at the canopy surface (r_X) is given as (Norman et al., 1995):

$$r_X = \frac{C'}{LAI} \left(\frac{l_w}{U_{d+z_M}} \right)^{1/2} \tag{A.4}$$

where C' is derived from weighting a coefficient in the equation for leaf boundary layer resistance over the height of the canopy, and the value is set to $90\ s^{1/2}\ m^{-1}$, LAI is leaf area index and it is given as Eq. (11) in the main body of the paper, l_w is effective leaf size, and it is given as 0.05 m in this paper as an observed mean size of the potato leaflets. In addition, U_{d+z_M} is the wind direction at the source-sink height ($d + z_M$) given as:

$$U_{d+z_M} = U_C e^{\left[-\mu \left(1 - \frac{d+z_M}{h_C} \right) \right]} \tag{A.5}$$

where U_C is wind speed at top of the canopy height (h_C), and it is given as:

$$U_C = U \left[\frac{\ln\left(\frac{h_C-d}{z_M}\right)}{\ln\left(\frac{z_U-d}{z_M}\right) - \psi_M} \right] \tag{A.6}$$

μ is calculated as:

$$\mu = 0.28F^{2/3} h_C^{1/3} S^{-1/3} \tag{A.7}$$

Appreciation is expressed to the Innovation Fund Denmark which funded two relevant projects: ERA-NET Co-fund Waterworks 2015 project ‘POTENTIAL’ - Variable rate irrigation and nitrogen fertilization in potato; Engage the spatial variation - and project ‘MOIST’ - Managing and optimizing irrigation by satellite tools - as well as the Graduate School of Technical Sciences at Aarhus University for financial support. The paper was also partly supported by the National Key Research and Development Program of China (2019YFE0125500-02) and Science and Technology Department of Guangdong Province (2019B020216001). Thanks to Joaquim Bellvert, Christian Jofre-Cekalovic and all of the colleagues in Efficient Use of Water in Agriculture Program, Institute of AgriFood, Research and Technology in Lleida, Spain for the help with data analysis and hosting of the first author’s international visit. Special thanks are also given to China Scholarship Council and S.C. Van Fonden for the financial support of the first author. The authors further would like to express appreciations to the anonymous reviewers for the constructive comments and suggestions for the paper improvement.

The equation for aerodynamic resistance at the soil surface (r_s) is given as (Kustas et al. 2016):

$$r_s = \frac{1}{0.0038(T_s - T_A)^{1/3} + 0.012U_s} \tag{A.8}$$

Where U_s is wind speed at a height (typically 0.05–0.2 m) above the soil surface where the effect of the soil surface roughness is minimal and it is given as:

$$U_s = U_C e^{\left(-\mu \left(1 - \frac{0.05}{h_C}\right)\right)} \tag{A.9}$$

Appendix B

The steps for the iterative process are (Norman et al., 1995):

- 1). initially estimate canopy temperature (T_C) as minimum of air temperature (T_A , which can be obtained from meteorological data) and radiometric temperature ($T_{rad}(\theta_o)$) which is land surface temperature (LST) retrieved from UAV thermal image.
- 2). calculate soil temperature (T_S) based on Eq. (6) since both of $T_{rad}(\theta_o)$ and T_C are known.
- 3). calculate net longwave radiation for canopy (Ln_C) and soil (Ln_S) with initial values of T_C and T_S . The calculations are shown in Appendix C.
- 4). calculate net radiation for canopy (Rn_C) as the sum of Ln_C and net shortwave radiation for canopy (Sn_C), likewise for net radiation for soil (Rn_S), which is the sum of Ln_S and net shortwave radiation for soil (Sn_S). The calculations are shown in Appendix C.
- 5). calculate canopy latent heat flux (LE_C) and canopy sensible heat flux (H_C) based on Eq. (10) and (2).

$$H_C = Rn_C - LE_C = Rn_C \left(1 - \alpha_{PT} f_g \frac{\Delta}{\Delta + \gamma}\right) \tag{B.1}$$

$$LE_C = Rn_C - H_C \tag{B.2}$$

where α_{PT} is the Priestley-Taylor coefficient initially set to 1.26, f_g is fraction of green canopy, Δ is the slope of saturation vapour pressure with temperature and γ is the psychrometric constant.

- 6). recalculate T_C .

Here, the T_C will be recalculated for the series resistance network. The linearized form of Eq. (6) in the main body of the paper is proposed to calculate $T_{C,lin}$ and small correction factor (ΔT_C).

T_C can be calculated as:

$$T_C = T_{C,lin} + \Delta T_C \tag{B.3}$$

$T_{C,lin}$ and ΔT_C are given as:

$$T_{C,lin} = \frac{\frac{T_A}{r_A} + \frac{T_{rad}(\theta_o)}{r_s[1-f_c(\theta_o)]} + \frac{H_C r_X}{\rho C_P} \left[\frac{1}{r_A} + \frac{1}{r_S} + \frac{1}{r_X}\right]}{\frac{1}{r_A} + \frac{1}{r_S} + \frac{f_c(\theta_o)}{r_X[1-f_c(\theta_o)]}} \tag{B.4}$$

$$\Delta T_C = \frac{T_{rad}^4(\theta_o) - f_c(\theta_o) T_{C,lin}^4 - [1 - f_c(\theta_o)] T_D^4}{4[1 - f_c(\theta_o)] T_D^3 \left(1 + \frac{r_S}{r_A}\right) + 4f_c(\theta_o) T_{C,lin}^3} \tag{B.5}$$

where r_A is surface resistance, r_X and r_S are the canopy and soil resistances and the calculation equations for r_A , r_X and r_S are shown in Appendix A, ρ is air density and C_P is the heat capacity of air, $f_c(\theta_o)$ is the fraction of vegetation observed by the thermal sensor and its calculation is shown in the main body of the paper, T_D is given as:

$$T_D = T_{C,lin} \left(1 + \frac{r_S}{r_A}\right) - \frac{H_C r_X}{\rho C_P} \left[1 + \frac{r_S}{r_X} + \frac{r_S}{r_A}\right] - T_A \frac{r_S}{r_A} \tag{B.6}$$

- 7). repeat step 2 to recalculate T_S and then recalculate r_S and T_{AC} ;

- 8). calculate H_S using Eq. (8), and G as:

$$G = 0.35Rn_S \tag{B.7}$$

- 9). Calculate LE_C and LE_S using Eqs. (2) and (3).

At this stage, the initial LE_S estimate is likely to yield negative-unrealistic values at daytime indicating dew condensation at soil surface. TSEB-PT then iteratively reduces α_{PT} in Eq. (10) in the main body of the paper and re-computes all temperatures and fluxes until realistic LE_S and LE_C are obtained (i.e. null or positive).

Appendix C

The net longwave radiation for canopy (Ln_C) and soil (Ln_S) are calculated by (Campbell and Norman, 2012):

$$Ln_C = (1 - e^{-k_t L A I})(L_{sky} + L_S - 2L_C) \tag{C.1}$$

$$Ln_S = e^{-k_L LAI} L_{sky} + (1 - e^{-k_L F}) L_C - L_S \tag{C.2}$$

where k_L is extinction coefficient for thermal radiation and it is set to 0.95, LAI is leaf area index and it is given as Eq. (11) in the main body of the paper, L_{sky} is the sky longwave irradiance, and it can be estimated from meteorological data, L_C and L_S are longwave emission from canopy and soil and the calculation equations are:

$$L_C = \epsilon_C \sigma T_C^4 \tag{C.3}$$

$$L_S = \epsilon_S \sigma T_S^4 \tag{C.4}$$

where ϵ_C and ϵ_S are emissivity of canopy (set as 0.98) and soil (set as 0.95), σ is Stephan-Boltzmann constant ($5.67037 \times 10^{-8} \text{ W m}^{-2} \text{ K}^{-4}$).

The net radiation for canopy (Rn_C) is the sum of Ln_C and net shortwave radiation for canopy (Sn_C), likewise for net radiation for soil (Rn_S), which is the sum of Ln_S and net shortwave radiation for soil (Sn_S). The equations are (Campbell and Norman, 2012):

$$Rn_C = Ln_C + Sn_C \tag{C.5}$$

$$Rn_S = Ln_S + Sn_S \tag{C.6}$$

The calculation equations for Sn_C and Sn_S are (Campbell and Norman, 2012):

$$Sn_C = (1 - \tau_{b,C,vis}) (1 - \beta_{b,C,vis}) S_b f_{vis} + (1 - \tau_{b,C,nir}) (1 - \beta_{b,C,nir}) S_b f_{nir} + (1 - \tau_{d,C,vis}) (1 - \beta_{d,C,vis}) S_d f_{vis} + (1 - \tau_{d,C,nir}) (1 - \beta_{d,C,nir}) S_d f_{nir} \tag{C.7}$$

$$Sn_S = \tau_{b,C,vis} (1 - v_{S,vis}) S_b f_{vis} + \tau_{b,C,nir} (1 - v_{S,nir}) S_b f_{nir} + \tau_{d,C,vis} (1 - v_{S,vis}) S_d f_{vis} + \tau_{d,C,nir} (1 - v_{S,nir}) S_d f_{nir} \tag{C.8}$$

where $\tau_{b,C,vis}$ and $\tau_{b,C,nir}$ are direct beam canopy transmittance in visible and near-infra red (NIR) regions, $\tau_{d,C,vis}$ and $\tau_{d,C,nir}$ are diffuse canopy transmittance in visible and NIR regions, $\beta_{b,C,vis}$ and $\beta_{b,C,nir}$ are direct beam canopy reflection coefficient (albedo) in visible and NIR regions, $\beta_{d,C,vis}$ and $\beta_{d,C,nir}$ are diffuse canopy albedo in visible and NIR regions, $v_{S,vis}$ and $v_{S,nir}$ are soil bi-hemispherical reflectances in the visible and NIR regions. S_b and S_d are incoming direct beam shortwave radiation and incoming diffuse shortwave radiation, f_{vis} and f_{nir} are potential fractions of total radiation in visible and NIR regions.

The calculation equation for beam canopy transmittance coefficient ($\tau_{b,c}$) are (regardless visible or NIR region):

$$\tau_{b,c} = \frac{[\beta_{b,c}^{*2} - 1] e^{-\sqrt{\phi k_{be}} \Omega LAI}}{(\beta_{b,c}^* v_S - 1) + \beta_{b,c}^* (\beta_{b,c}^* - v_S) e^{-2\sqrt{\phi k_{be}} \Omega LAI}} \tag{C.9}$$

where Ω is solar angular clumping index which is calculated assuming potato is a row crop with row direction set at 330° and its calculation was shown in Appendix B1 from Nieto et al. (2019). v_S is soil bi-hemispherical reflectance, and its values in visible region (400–700 nm) and near-infra red (NIR, 700–2500 nm) region are set as 0.15 and 0.25 according to the empirical estimation. ϕ is leaf absorptivity, and it is given as:

$$\phi = 1 - v_C - \tau_C \tag{C.10}$$

where v_C is leaf bi-hemispherical reflectance and its values in visible and NIR regions are set as 0.07 and 0.32, τ_C is leaf bi-hemispherical transmittance and its values in visible NIR regions are set as 0.08 and 0.33 based on empirical estimation.

$\beta_{b,c}^*$ is beam canopy reflection coefficient for a deep canopy, and it is given as:

$$\beta_{b,c}^* = \frac{2k_{be}}{k_{be} + 1} \beta_C \tag{C.11}$$

where β_C is canopy hemispherical reflection coefficient and it is given as:

$$\beta_C = \frac{1 - \sqrt{\phi}}{1 + \sqrt{\phi}} \tag{C.12}$$

Beam canopy reflection coefficient ($\beta_{b,c}$) for a generic canopy is given by:

$$\beta_{b,c} = \frac{\beta_{b,c}^* + \left[\frac{\beta_{b,c}^* - v_S}{\beta_{b,c}^* v_S - 1} \right] e^{-2\sqrt{\phi k_{be}} \Omega LAI}}{1 + \beta_{b,c}^* \left[\frac{\beta_{b,c}^* - v_S}{\beta_{b,c}^* v_S - 1} \right] e^{-2\sqrt{\phi k_{be}} \Omega LAI}} \tag{C.13}$$

It should be noted that in this paper, the potato canopy is assumed as generic canopy.

The calculation equation for diffuse canopy transmittance coefficient ($\tau_{d,c}$) is:

$$\tau_{d,c} = \frac{[\beta_{d,c}^{*2} - 1] e^{-\sqrt{\phi k_d} LAI}}{(\beta_{d,c}^* v_S - 1) + \beta_{d,c}^* (\beta_{d,c}^* - v_S) e^{-2\sqrt{\phi k_d} LAI}} \tag{C.14}$$

k_d is diffuse extinction coefficient and it is given as:

$$k_d = \frac{-\ln \sum_{\theta_s=0}^{90} (5 \cos \theta_s \sin \theta_s e^{-k_{bc}(\theta_s) LAI})}{F} \tag{C.15}$$

where θ_s is solar zenith angle and its calculation method is present in the main body of this paper and it ranges from 0 to 90 with interval 5.

$\beta_{d,C}^*$ is beam canopy reflection coefficient for a deep canopy, and it is given as:

$$\beta_{d,C}^* = \frac{2k_d}{k_d + 1} \beta_C \tag{C.16}$$

Diffuse canopy reflection coefficient $\beta_{d,C}$ for a generic canopy is given by:

$$\beta_{d,C} = \frac{\beta_{d,C}^* + \left[\frac{\beta_{d,C}^* - v_S}{\beta_{d,C}^* v_S - 1} \right] e^{-2\sqrt{\phi k_d LAI}}}{1 + \beta_{d,C}^* \left[\frac{\beta_{d,C}^* - v_S}{\beta_{d,C}^* v_S - 1} \right] e^{-2\sqrt{\phi k_d LAI}}} \tag{C.17}$$

S_b and S_d are given as (Weiss and Norman, 1985):

$$S_b = S(1 - \xi_d) \tag{C.18}$$

$$S_d = S\xi_d \tag{C.19}$$

where S is incoming shortwave radiation ($W m^{-2}$) and it can be obtained from meteorological data, and ξ_d is diffusion coefficient, and it is given as:

$$\xi_d = f_{d,vis} f_{vis} + f_{d,nir} f_{nir} \tag{C.20}$$

where f_{vis} and f_{nir} are given as:

$$f_{vis} = \frac{R_{b,vis} + R_{d,vis}}{R_{b,vis} + R_{d,vis} + R_{b,nir} + R_{d,nir}} \tag{C.21}$$

$$f_{nir} = \frac{R_{b,nir} + R_{d,nir}}{R_{b,vis} + R_{d,vis} + R_{b,nir} + R_{d,nir}} \tag{C.22}$$

where $R_{b,vis}$ and $R_{d,vis}$ are potential beam (direct) and diffuse radiation in visible region, and $R_{b,nir}$ and $R_{d,nir}$ are potential beam and diffuse radiation in NIR region. The equations are shown as:

$$R_{b,vis} = GSC f_{e,vis} e^{(-0.185 \frac{P_A}{P_0} m)} \cos \theta_s \tag{C.23}$$

$$R_{d,vis} = 0.4(GSC f_{e,vis} - R_{b,vis}) \cos \theta_s \tag{C.24}$$

$$R_{b,nir} = (GSC f_{e,nir} e^{-0.06 \frac{P_A}{P_0} m} - w) \cos \theta_s \tag{C.25}$$

$$R_{d,nir} = 0.6(GSC f_{e,nir} - R_{b,nir} - w) \cos \theta_s \tag{C.26}$$

where GCS is solar constant and its value is $1320 W m^{-2}$, $f_{e,vis}$ and $f_{e,nir}$ are empirical fraction of radiation in the visible and NIR regions and they are set as 0.4545 and 0.5455, P_A is actual air pressure and it can be obtained from the meteorological data, P_0 is the air pressure at sea level and it is set as 1013.25 mbar, m is optical air mass and it is given by:

$$m = \frac{1}{\cos \theta_s} \tag{C.27}$$

w is the water absorption in the NIR region for 10 mm of precipitation water and it is given as:

$$w = GSC 10^{-1.195 + 0.4459 \log_{10} m - 0.0345 \log_{10} m^2} \tag{C.28}$$

$f_{d,vis}$ and $f_{d,nir}$ are diffuse fractions in visible and NIR regions, and they are given as:

$$f_{d,vis} = 1 - \frac{R_{b,vis}}{R_{b,vis} + R_{d,vis}} \left[1 - \left(\frac{0.9 - \Phi}{0.7} \right)^{\frac{2}{3}} \right] \tag{C.29}$$

$$f_{d,nir} = 1 - \frac{R_{b,nir}}{R_{b,nir} + R_{d,nir}} \left[1 - \left(\frac{0.88 - \Phi}{0.68} \right)^{\frac{2}{3}} \right] \tag{C.30}$$

where Φ represents the ratio of measured to potential shortwave radiation and it is given as:

$$\Phi = \frac{SR}{R_{b,vis} + R_{d,vis} + R_{b,nir} + R_{d,nir}} \tag{C.31}$$

Appendix D. Supplementary material

Supplementary data to this article can be found online at <https://doi.org/10.1016/j.isprsjprs.2023.03.009>.

References

- Allen, R.G., Pereira, L.S., Raes, D., Smith, M., 2012. Crop evapotranspiration-Guidelines for computing crop water requirements-FAO Irrigation and drainage paper 56, 300. Fao, Rome, p. D05109.
- Andersen, M., Jensen, C., Losch, R., 1991. Derivation of pressure-volume curves by a non-linear regression procedure and determination of apoplastic water. *J. Exp. Bot.* 42, 159–165.
- Andersen, M.C., Kustas, W.P., Norman, J.M., Hain, C.R., Mecikalski, J.R., Schultz, L., González-Dugo, M., Cammalleri, C., d'Urso, G., Pimstein, A., 2011. Mapping daily evapotranspiration at field to continental scales using geostationary and polar orbiting satellite imagery. *Hydrol. Earth Syst. Sci.* 15 (1), 223–239.
- Anderson, M.C., Norman, J.M., Mecikalski, J.R., Torn, R.D., Kustas, W.P., Basara, J.B., 2004. A multiscale remote sensing model for disaggregating regional fluxes to micrometeorological scales. *J. Hydrometeorol.* 5, 343–363.
- Anderson, G., Peng, R., 2012. weathermetrics: Functions to convert between weather metrics (R package). The R Project for Statistical Computing.
- Andreu, A., Kustas, W.P., Polo, M.J., Carrara, A., González-Dugo, M.P., 2018. Modeling surface energy fluxes over a dehesa (oak savanna) ecosystem using a thermal based two-source energy balance model (TSEB) I. *Remote Sens. (Basel)* 10, 567.
- Antoniuk, V., Manevski, K., Krup, K., Larsen, R., Andersen, M.N., 2021. Diurnal and Seasonal Mapping of Water Deficit Index and Evapotranspiration by an Unmanned Aerial System: A Case Study for Winter Wheat in Denmark. *Remote Sens. (Basel)* 13, 2998.
- Aubrecht, D.M., Helliker, B.R., Goulden, M.L., Roberts, D.A., Still, C.J., Richardson, A.D., 2016. Continuous, long-term, high-frequency thermal imaging of vegetation: Uncertainties and recommended best practices. *Agric. For. Meteorol.* 228, 315–326.
- Bellvert, J., Jofre-Čekalović, C., Pelechá, A., Mata, M., Nieto, H., 2020. Feasibility of using the two-source energy balance model (TSEB) with Sentinel-2 and Sentinel-3 images to analyze the spatio-temporal variability of vine water status in a vineyard. *Remote Sens. (Basel)* 12, 2299.
- Berg, A., Lintner, B.R., Findell, K., Seneviratne, S.I., van den Hurk, B., Ducharne, A., Chéry, F., Hagemann, S., Lawrence, D.M., Malyshev, S., 2015. Interannual coupling between summertime surface temperature and precipitation over land: Processes and implications for climate change. *J. Clim.* 28, 1308–1328.
- Bhatia, S.C., 2014. 2 - Solar radiations. In: Bhatia, S.C. (Ed.), *Advanced Renewable Energy Systems*. Woodhead Publishing India, pp. 32–67.
- Blum, A., 2009. Effective use of water (EUW) and not water-use efficiency (WUE) is the target of crop yield improvement under drought stress. *Field Crop Res* 112, 119–123.
- Brutsaert, W., 2005. *Hydrology: an introduction*. Cambridge University Press.
- Burchard-Levine, V., Nieto, H., Riaño, D., Migliavacca, M., El-Madany, T.S., Guzinski, R., Carrara, A., Martín, M.P., 2021. The effect of pixel heterogeneity for remote sensing based retrievals of evapotranspiration in a semi-arid tree-grass ecosystem. *Remote Sens. Environ.* 260, 112440.
- Cammalleri, C., Anderson, M.C., Kustas, W.P., 2014. Upscaling of evapotranspiration fluxes from instantaneous to daytime scales for thermal remote sensing applications. *Hydrol. Earth Syst. Sci.* 18, 1885–1894.
- Campbell, G.S., Norman, J., 2012. *An introduction to environmental biophysics*. Springer Science & Business Media.
- Christensen, S., Goudriaan, J., 1993. Deriving light interception and biomass from spectral reflectance ratio. *Remote Sens. Environ.* 43, 87–95.
- Colaizzi, P.D., Evett, S.R., Howell, T.A., Li, F., Kustas, W.P., Anderson, M.C., 2012. Radiation model for row crops: I. Geometric view factors and parameter optimization. *Agron. J.* 104, 225–240.
- Crosby, T.W., Wang, Y., 2021. Effects of Irrigation Management on Chipping Potato (*Solanum tuberosum* L.) Production in the Upper Midwest of the U.S. *Agronomy* 11, 768.
- Dalla Costa, L., Delle Vedove, G., Gianquinto, G., Giovanardi, R., Peressotti, A., 1997. Yield, water use efficiency and nitrogen uptake in potato: influence of drought stress. *Potato Res.* 40, 19–34.
- Fisher, J.B., Malhi, Y., Bonal, D., Da Rocha, H.R., De Araújo, A.C., Gamo, M., Goulden, M.L., Hirono, T., Huete, A.R., Kondo, H., Kumagai, T.O., Loescher, H.W., Miller, S., Nobre, A.D., Nouvellon, Y., Oberbauer, S.F., Panuthai, S., Rouspard, O., Saleska, S., Tanaka, K., Tanaka, N., Tu, K.P., Von Randow, C., 2009. The land-atmosphere water flux in the tropics. *Glob. Chang. Biol.* 15, 2694–2714.
- Fitter, A., Hay, R., 2002. 2 - Energy and Carbon. In: Fitter, A., Hay, R. (Eds.), *Environmental Physiology of Plants*, Third Edition. Academic Press, London, pp. 23–73.
- García-Tejera, O., López-Bernal, Á., Orgaz, F., Testi, L., Villalobos, F.J., 2021. The pitfalls of water potential for irrigation scheduling. *Agric Water Manag* 243, 106522.
- Gowda, P.H., Chavez, J.L., Colaizzi, P.D., Evett, S.R., Howell, T.A., Tolk, J.A., 2008. ET mapping for agricultural water management: present status and challenges. *Irrig. Sci.* 26, 223–237.
- Grossiord, C., Buckley, T.N., Cernusak, L.A., Novick, K.A., Poulter, B., Siegwolf, R.T.W., Sperry, J.S., McDowell, N.G., 2020. Plant responses to rising vapor pressure deficit. *New Phytol.* 226, 1550–1566.
- Guzinski, R., Nieto, H., 2019. Evaluating the feasibility of using Sentinel-2 and Sentinel-3 satellites for high-resolution evapotranspiration estimations. *Remote Sens. Environ.* 221, 157–172.
- Hijmans, R.J., 2003. The effect of climate change on global potato production. *Am. J. Potato Res.* 80, 271–279.
- Hillel, D., 2003. *Introduction to environmental soil physics*. Elsevier.
- Hoffmann, H., Nieto, H., Jensen, R., Guzinski, R., Zarco-Tejada, P., Friborg, T., 2016. Estimating evaporation with thermal UAV data and two-source energy balance models. *Hydrol. Earth Syst. Sci.* 20, 697–713.
- Hsiao, T.C., Acevedo, E., 1975. Plant responses to water deficits, water-use efficiency, and drought resistance. In: *Developments in Agricultural and Managed Forest Ecology*. Elsevier, pp. 59–84.
- Jensen, C., Svendsen, H., Andersen, M., Lösch, R., 1993. Use of the root contact concept, an empirical leaf conductance model and pressure-volume curves in simulating crop water relations. *Plant and Soil* 149, 1–26.
- Katerji, N., Hallaire, M., Menoux-Boyer, Y., Durand, B., 1986. Modelling diurnal patterns of leaf water potential in field conditions. *Ecol. Model.* 33, 185–203.
- Kirda, C., Topcu, S., Kaman, H., Ulger, A., Yazici, A., Cetin, M., Derici, M., 2005. Grain yield response and N-fertiliser recovery of maize under deficit irrigation. *Field Crop Res* 93, 132–141.
- Knipper, K.R., Kustas, W.P., Anderson, M.C., Alfieri, J.G., Prueger, J.H., Hain, C.R., Gao, F., Yang, Y., McKee, L.G., Nieto, H., Hipps, L.E., Alsina, M.M., Sanchez, L., 2019. Evapotranspiration estimates derived using thermal-based satellite remote sensing and data fusion for irrigation management in California vineyards. *Irrig. Sci.* 37, 431–449.
- Kustas, W., Anderson, M., 2009. Advances in thermal infrared remote sensing for land surface modeling. *Agric. For. Meteorol.* 149, 2071–2081.
- Kustas, W.P., Norman, J.M., 1999. Evaluation of soil and vegetation heat flux predictions using a simple two-source model with radiometric temperatures for partial canopy cover. *Agric. For. Meteorol.* 94, 13–29.
- Lee, S.S., Donner, L.J., Phillips, V., 2009. Sensitivity of aerosol and cloud effects on radiation to cloud types: comparison between deep convective clouds and warm stratiform clouds over one-day period. *Atmos. Chem. Phys.* 9, 2555–2575.
- Lesk, C., Coffel, E., Winter, J., Ray, D., Zscheischler, J., Seneviratne, S.I., Horton, R., 2021. Stronger temperature-moisture couplings exacerbate the impact of climate warming on global crop yields. *Nature Food* 2, 683–691.
- Leuning, R., Kelliher, F.M., De Pury, D.G.G., Schulze, E.D., 1995. Leaf nitrogen, photosynthesis, conductance and transpiration: scaling from leaves to canopies. *Plant Cell Environ.* 18, 1183–1200.
- Li, F., Kustas, W.P., Anderson, M.C., Prueger, J.H., Scott, R.L., 2008. Effect of remote sensing spatial resolution on interpreting tower-based flux observations. *Remote Sens. Environ.* 112, 337–349.
- Li, X., Xu, X., Wang, X., Xu, S., Tian, W., Tian, J., He, C., 2021. Assessing the effects of spatial scales on regional evapotranspiration estimation by the SEBAL model and multiple satellite datasets: a case study in the agro-pastoral ecotone, Northwestern China. *Remote Sensing* 13, 1524.
- Li, G., Zhang, F., Jing, Y., Liu, Y., Sun, G., 2017. Response of evapotranspiration to changes in land use and land cover and climate in China during 2001–2013. *Sci. Total Environ.* 596–597, 256–265.
- Lisovski, S., Wotherspoon, S., Sumner, M., Bauer, S., Emmenegger, T., Lisovski, M.S., 2015. Package 'GeoLight'. The R Project for Statistical Computing.
- Liu, F., Andersen, M.N., Jacobsen, S.-E., Jensen, C.R., 2005a. Stomatal control and water use efficiency of soybean (*Glycine max* L. Merr.) during progressive soil drying. *Environ. Exp. Bot.* 54, 33–40.
- Liu, F., Jensen, C.R., Shahanzari, A., Andersen, M.N., Jacobsen, S.-E., 2005b. ABA regulated stomatal control and photosynthetic water use efficiency of potato (*Solanum tuberosum* L.) during progressive soil drying. *Plant Sci.* 168, 831–836.
- Liu, F., Shahnazari, A., Andersen, M., Jacobsen, S.-E., Jensen, C., 2006a. Effects of deficit irrigation (DI) and partial root drying (PRD) on gas exchange, biomass partitioning, and water use efficiency in potato. *Sci. Hortic.* 109, 113–117.
- Liu, F., Shahnazari, A., Andersen, M.N., Jacobsen, S.-E., Jensen, C.R., 2006b. Physiological responses of potato (*Solanum tuberosum* L.) to partial root-zone drying: ABA signalling, leaf gas exchange, and water use efficiency. *J. Exp. Bot.* 57 (14), 3727–3735.
- Lobell, D.B., Bonfils, C.J., Kueppers, L.M., Snyder, M.A., 2008. Irrigation cooling effect on temperature and heat index extremes. *Geophys. Res. Lett.* 35.
- Lobell, D.B., Hammer, G.L., McLean, G., Messina, C., Roberts, M.J., Schlenker, W., 2013. The critical role of extreme heat for maize production in the United States. *Nat. Clim. Chang.* 3, 497–501.
- Maes, W.H., Steppe, K., 2012. Estimating evapotranspiration and drought stress with ground-based thermal remote sensing in agriculture: a review. *J. Exp. Bot.* 63, 4671–4712.
- Mallick, K., Bhattacharya, B., Rao, V.U.M., Reddy, D., Banerjee, S., Venkatesh, H., Pandey, V., Kar, G., Mukherjee, J., Vyas, S., Gadgil, A., Patel, N.K., 2009. Latent heat flux estimation in clear sky days over Indian agroecosystems using noontime satellite remote sensing data. *Agric. For. Meteorol.* 149, 1646–1665.

- Meier, F., Scherer, D., Richters, J., Christen, A., 2011. Atmospheric correction of thermal-infrared imagery of the 3-D urban environment acquired in oblique viewing geometry. *Atmos. Meas. Tech.* 4, 909–922.
- Mesas-Carrascosa, F.-J., Pérez-Porrás, F., Meroño de Larriva, J.E., Mena Frau, C., Agüera-Vega, F., Carvajal-Ramírez, F., Martínez-Carricondo, P., García-Ferrer, A., 2018. Drift correction of lightweight microbolometer thermal sensors on-board unmanned aerial vehicles. *Remote Sens. (Basel)* 10, 615.
- Morillas, L., García, M., Nieto, H., Villagarcía, L., Sandholt, I., Gonzalez-Dugo, M., Zarco-Tejada, P., Domingo, F., 2013. Using radiometric surface temperature for surface energy flux estimation in Mediterranean drylands from a two-source perspective. *Remote Sens. Environ.* 136, 234–246.
- Nassar, A., Torres-Rua, A., Kustas, W., Alfieri, J., Hipps, L., Prueger, J., Nieto, H., Alsina, M.M., White, W., McKee, L., Coopmans, C., Sanchez, L., Dokoozlian, N., 2021. Assessing daily evapotranspiration methodologies from one-time-of-day sUAS and EC information in the GRAPEX project. *Remote Sens. (Basel)* 13, 2887.
- Nieto, H., Kustas, W.P., Torres-Rúa, A., Alfieri, J.G., Gao, F., Anderson, M.C., White, W. A., Song, L., Del Mar Alsina, M., Prueger, J.H., McKee, M., Elarab, M., McKee, L.G., 2019. Evaluation of TSEB turbulent fluxes using different methods for the retrieval of soil and canopy component temperatures from UAV thermal and multispectral imagery. *Irrig. Sci.* 37, 389–406.
- Norman, J.M., Kustas, W.P., Humes, K.S., 1995. Source approach for estimating soil and vegetation energy fluxes in observations of directional radiometric surface temperature. *Agric. For. Meteorol.* 77, 263–293.
- Obidiegwu, J.E., Bryan, G.J., Jones, H.G., Prashar, A., 2015. Coping with drought: stress and adaptive responses in potato and perspectives for improvement. *Front. Plant Sci.* 6, 542.
- Olbrycht, R., Więcek, B., De Mey, G., 2012. Thermal drift compensation method for microbolometer thermal cameras. *Appl. Opt.* 51, 1788–1794.
- Olesen, J.E., & Plauborg, F.L. (1995). *MVTOOL version 1.10 for developing MARKVAND*. Pallardy, S.G., 2008. CHAPTER 5 - Photosynthesis. In: Pallardy, S.G. (Ed.), *Physiology of Woody Plants*, Third Edition. Academic Press, San Diego, pp. 107–167.
- Parry, C.K., Nieto, H., Guillevic, P., Agam, N., Kustas, W.P., Alfieri, J., McKee, L., McElrone, A.J., 2019. An intercomparison of radiation partitioning models in vineyard canopies. *Irrig. Sci.* 37, 239–252.
- Peng, J., Manevski, K., Kørup, K., Larsen, R., Zhou, Z., Andersen, M.N., 2021a. Environmental constraints to net primary productivity at northern latitudes: A study across scales of radiation interception and biomass production of potato. *Int. J. Appl. Earth Obs. Geoinf.* 94, 102232.
- Peng, J., Manevski, K., Sørensen, K., Larsen, R., Andersen, M., 2021b. Random forest regression results in accurate assessment of potato nitrogen status based on multispectral data from different platforms and the critical concentration approach. *Field Crop Res* 268, 108158.
- Pérez, G., Coma, J., 2018. Chapter 3.10 - Vertical Greening Systems to Improve Water Management. In: Pérez, G., Perini, K. (Eds.), *Nature Based Strategies for Urban and Building Sustainability*. Butterworth-Heinemann, pp. 191–201.
- Priestley, C.H.B., Taylor, R.J., 1972. On the assessment of surface heat flux and evaporation using large-scale parameters. *Mon. Weather Rev.* 100, 81–92.
- Razzaghi, F., Plauborg, F., Jacobsen, S.-E., Jensen, C.R., Andersen, M.N., 2012. Effect of nitrogen and water availability of three soil types on yield, radiation use efficiency and evapotranspiration in field-grown quinoa. *Agric Water Manag* 109, 20–29.
- Shahnazari, A., Liu, F., Andersen, M., Jacobsen, S.-E., Jensen, C., 2007. Effects of partial root-zone drying on yield, tuber size and water use efficiency in potato under field conditions. *Field Crop Res* 100, 117–124.
- Steduto, P., Hsiao, T.C., Fereres, E., Raes, D., 2012. *Crop yield response to water*, 1028. Fao, Rome, p. 99.
- Taiz, L., Zeiger, E., 2010. *Plant physiology*, 5th edn Sunderland. Sinauer Associates. [Google Scholar], MA.
- Team, R.C. (2013). *R: A language and environment for statistical computing*.
- Teskey, R., Werten, T., Bauweraerts, I., Ameye, M., McGuire, M.A., Steppe, K., 2015. Responses of tree species to heat waves and extreme heat events. *Plant Cell Environ.* 38, 1699–1712.
- Thomsen, A. (1994). Program AUTOTDR for making automated TDR measurements of soil water content. In: *User's Guide*. Tjele, Denmark: Danish Institute of Agricultural Sciences.
- Thysen, I., Detlefsen, N.K., 2006. Online decision support for irrigation for farmers. *Agric Water Manag* 86, 269–276.
- Timlin, D., Lutfur Rahman, S., Baker, J., Reddy, V., Fleisher, D., Quebedeaux, B., 2006. Whole plant photosynthesis, development, and carbon partitioning in potato as a function of temperature. *Agron. J.* 98, 1195–1203.
- Trout, T.J., Howell, T.A., English, M.J., Martin, D.L., 2020. Deficit irrigation strategies for the Western U.S. *Trans. ASABE* 63, 1813–1825.
- Twine, T.E., Kustas, W.P., Norman, J.M., Cook, D.R., Houser, P.R., Meyers, T.P., Prueger, J.H., Starks, P.J., Wesely, M.L., 2000. Correcting eddy-covariance flux underestimates over a grassland. *Agric. For. Meteorol.* 103, 279–300.
- Verhoef, A., De Bruin, H., Van Den Hurk, B., 1997. Some practical notes on the parameter $k_B - 1$ for sparse vegetation. *J. Appl. Meteorol.* 36, 560–572.
- Wada, Y., van Beek, L.P.H., van Kempen, C.M., Reckman, J.W.T.M., Vasak, S., Bierkens, M.F.P., 2010. Global depletion of groundwater resources. *Geophys. Res. Lett.* 37.
- Wang, X., 2015. Vapor flow resistance of dry soil layer to soil water evaporation in arid environment: An overview. *Water* 7, 4552–4574.
- Wang, S., Garcia, M., Bauer-Gottwein, P., Jakobsen, J., Zarco-Tejada, P.J., Bandini, F., Paz, V.S., Ibrom, A., 2019. High spatial resolution monitoring land surface energy, water and CO₂ fluxes from an Unmanned Aerial System. *Remote Sens. Environ.* 229, 14–31.
- Weiss, A., Norman, J.M., 1985. Partitioning solar radiation into direct and diffuse, visible and near-infrared components. *Agric. For. Meteorol.* 34, 205–213.
- Xia, T., Kustas, W.P., Anderson, M.C., Alfieri, J.G., Gao, F., McKee, L., Prueger, J.H., Geli, H.M.E., Neale, C.M.U., Sanchez, L., Alsina, M.M., Wang, Z., 2016. Mapping evapotranspiration with high-resolution aircraft imagery over vineyards using one- and two-source modeling schemes. *Hydrol. Earth Syst. Sci.* 20, 1523–1545.
- Xue, F., Liu, W., Cao, H., Song, L., Ji, S., Tong, L., Ding, R., 2021. Stomatal conductance of tomato leaves is regulated by both abscisic acid and leaf water potential under combined water and salt stress. *Physiol. Plant*.
- Yao, Y., Liang, S., Li, X., Chen, J., Wang, K., Jia, K., Cheng, J., Jiang, B., Fisher, J.B., Mu, Q., Grünwald, T., Bernhofer, C., Rounsard, O., 2015. A satellite-based hybrid algorithm to determine the Priestley-Taylor parameter for global terrestrial latent heat flux estimation across multiple biomes. *Remote Sens. Environ.* 165, 216–233.
- Yoo, C.Y., Pence, H.E., Hasegawa, P.M., Mickelbart, M.V., 2009. Regulation of transpiration to improve crop water use. *Crit. Rev. Plant Sci.* 28, 410–431.
- Zhang, P., Yang, X., Manevski, K., Li, S., Wei, Z., Andersen, M.N., Liu, F., 2022. Physiological and growth responses of potato (*Solanum Tuberosum* L.) to air temperature and relative humidity under soil water deficits. *Plants* 11, 1126.
- Zhou, Z., Plauborg, F., Kristensen, K., Andersen, M.N., 2017. Dry matter production, radiation interception and radiation use efficiency of potato in response to temperature and nitrogen application regimes. *Agric. For. Meteorol.* 232, 595–605.
- Zhou, Z., Jabloun, M., Plauborg, F., Andersen, M.N., 2018. Using ground-based spectral reflectance sensors and photography to estimate shoot N concentration and dry matter of potato. *Comput. Electron. Agric.* 144, 154–163.